ARTICLE OPEN

Robust neurogenesis in chronic stroke monkeys following mesenchymal stem cell transplantation plus intermittent theta-burst stimulation

Yuan-Huan Ma[1,2,3], Geng-Bin Chen[1], Man-Feng Wu[1], Ge Li[4], Yu Zhang[4], Jian-Ping Lv[5], Min Wen[5], Lei Cai[4], Cai-Ling Zhang[1], Jun-Bo Jiang[1], Ke Zhang[6], Ke-Jun Zhang[7], Ying Liu[7], Zhou Liu[3], Jia-Lin Chen[1], Tuo Lin[1], Li-Xin Wang[8], Guang-Qing Xu[9]✉, Xiang Zeng[7]✉ and Yue Lan[1]✉

A significant population of chronic stroke patients urgently requires more effective therapies because of functional plateaus and limited intervention options. Intermittent theta-burst stimulation (iTBS) has been increasingly adopted in chronic-phase ischemic stroke management. However, the efficacy decreases over time. Mesenchymal stem cells (MSCs) have emerged as a promising therapeutic strategy for chronic stroke management through multiple mechanisms. Whether combined MSC transplantation and iTBS confers superior synergistic efficacy warrants further investigation. In this study, human umbilical cord-derived MSCs were stereotactically injected into the penumbra of the brain parenchyma adjacent to infarct sites in cynomolgus monkeys with chronic-stage middle cerebral artery occlusion (MCAO)-induced ischemic stroke. iTBS commenced at 1 week post-transplantation (5 sessions/week until week 17). Behavioral tests, electrophysiological recordings, functional magnetic resonance imaging (fMRI), magnetic resonance spectroscopy (MRS), and plasma proteomic analysis were conducted longitudinally, with terminal histological and spatial proteomic analysis at week 17. The results indicated that combined MSC/iTBS therapy enhanced motor function, reduced cortical excitation thresholds, shortened motor-evoked potential (MEP) latency, increased neural activity intensity/synchronization, strengthened functional connectivity, and optimized motor cortex metabolism. In addition to the commonly attributed therapeutic mechanisms of MSCs and iTBS, the combined therapy additionally triggered neurogenesis and stem cell chemotaxis, which was potentially mediated by iTBS-enhanced CXCL12 secretion from MSCs. Therefore, MSC/iTBS combination therapy can effectively treat chronic stroke through multiple mechanisms, particularly involving the activation of endogenous neural stem cells (NSCs), representing a promising interdisciplinary treatment strategy.

Signal Transduction and Targeted Therapy (2026)11:153 ; https://doi.org/10.1038/s41392-026-02694-5

INTRODUCTION

Ischemic stroke, also known as cerebral infarction, is a prevalent condition with a high incidence and significant disability rate. It has emerged as a major global public health challenge, impacting millions of individuals and imposing a substantial burden on society and the families of those affected.[1] Stroke is recognized as the third leading cause of mortality worldwide and the fourth leading cause of disability-adjusted life-years (DALYs), which quantify the overall disease burden by combining both premature death and disability due to illness.[2] Approximately 50% to 80% of individuals poststroke experience upper limb dysfunction, with the majority confronting long-term disability challenges.[3] Consequently, enhancing motor function in stroke survivors, improving their quality of life, and alleviating the societal burden represent acute medical priorities. With the ongoing refinements in stroke treatment technology, there has been a significant reduction in stroke-related mortality rates.[4] Concurrently, the incidence of individuals transitioning into the chronic phase of stroke has been on an upward trajectory. The initial six months post-stroke are often regarded as the critical period for optimal functional recovery in patients.[5] Beyond this acute phase and upon entering the chronic stage, the prospects for functional improvement have

[1]Department of Rehabilitation Medicine, School of Medicine, the Second Affiliated Hospital of South China University of Technology (Guangzhou First People's Hospital), Guangzhou, China; [2]Center for Stem Cell Biology and Tissue Engineering, Key Laboratory for Stem Cells and Tissue Engineering Ministry of Education, Department of Histoembryology and Cell Biology, Zhongshan School of Medicine, Sun Yat-sen University, Guangzhou, China; [3]Guangdong Key Laboratory of Age-Related Cardiac and Cerebral Diseases, Institute of Neurology, Affiliated Hospital of Guangdong Medical University, Zhanjiang, China; [4]Guangdong Provincial Biotechnology Research Institute (Guangdong Provincial Laboratory Animals Monitoring Center), Guangzhou, China; [5]Department of Neurosurgery, School of Medicine, The Second Affiliated Hospital of South China University of Technology (Guangzhou First People's Hospital), Guangzhou, China; [6]State Key Laboratory of Quality Research in Chinese Medicine, Institute of Chinese Medical Sciences, University of Macau, Macao, China; [7]Lab of Stem Cell Biology and Innovative Research of Chinese Medicine, National Institute of Stem Cell Clinical Research, Guangdong Provincial Key Laboratory of Chinese Medicine for Prevention and Treatment of Refractory Chronic Diseases, Guangdong Provincial Hospital of Chinese Medicine/Guangdong Academy of Chinese Medicine/The Second Affiliated Hospital of Guangzhou University of Chinese Medicine, Guangzhou, China; [8]Department of Neurocritical Care, The Second Affiliated Hospital of Guangzhou University of Chinese Medicine, Guangzhou, China and [9]Department of Rehabilitation Medicine, Guangdong Provincial People's Hospital (Guangdong Academy of Medical Sciences), Southern Medical University, Guangzhou, China
Correspondence: Guang-Qing Xu (guangchingx@163.com) or Xiang Zeng (zengxiang@gzucm.edu.cn) or Yue Lan (bluemooning@163.com)
These authors contributed equally: Yuan-Huan Ma, Geng-Bin Chen, Man-Feng Wu

Received: 3 July 2025 Revised: 30 January 2026 Accepted: 15 March 2026
Published online: 24 April 2026

become increasingly challenging.[6] Therefore, the substantial population of patients with chronic stroke urgently requires more effective treatments.

Currently, rehabilitation therapy based on neuroregulatory technology is widely used to treat chronic stroke. Transcranial magnetic stimulation (TMS), a noninvasive neuromodulatory rehabilitation therapy that modulates the excitability of neurons at the site of stimulation, thereby influencing brain functional connectivity and plasticity, has demonstrated its efficacy in the treatment of stroke patients by promoting neural recovery and enhancing rehabilitative outcomes.[7–9] TMS has a variety of regimens depending on the stimulation paradigm; for example, theta burst stimulation (TBS) is an advanced method of transcranial magnetic stimulation that was first introduced in 2005.[10] TBS consists of three high-frequency pulses delivered at 50 Hz every 200 ms, typically within a cluster, mimicking the brain's natural oscillatory activity.[11] Compared with rTMS, TBS has the advantages of a shorter stimulation time and lower stimulation intensity.[12] On the basis of the stimulation pattern, TBS is categorized into two distinct modes: continuous theta burst stimulation (cTBS), which typically exerts inhibitory effects on cortical excitability, and intermittent theta burst stimulation (iTBS), which generally enhances cortical excitability.[10] Given its facilitatory effect, the iTBS mode has garnered significant interest in stroke rehabilitation. A recent meta-analysis suggested that the iTBS stimulation mode appeared to be a more appropriate rTMS treatment strategy for upper limb dysfunction in chronic stroke patients.[13] Indeed, studies have shown that iTBS can increase the expression of neurotrophic factors to mediate neural stem cell (NSC) maturation and synaptic plasticity.[14,15] Additionally, iTBS can suppress neuroinflammation by modulating microglial polarization, reducing the levels of proinflammatory cytokines, such as IL-1β and TNF-α, and increasing the levels of the anti-inflammatory cytokine IL-10.[16] and decreasing IBA-1 and CD68 inflammatory cell populations.[17] This evidence highlights the potential therapeutic mechanism of iTBS in the clinic. However, evidence that TMS can improve motor dysfunction in the chronic phase of stroke (> 6 months) is insufficient.[18,19] Therefore, more therapeutic strategies with therapeutic effectiveness need to be developed to treat patients with chronic stroke.

Stem cell-based cell therapies, particularly those involving mesenchymal stem cell (MSC) transplantation, are emerging as highly promising strategies for the treatment of stroke. The potential of MSCs to modulate neuroinflammation, promote neuroprotection and improve neurological function has garnered significant interest in stroke treatment.[20,21] For example, clinical studies have shown significant improvements in neurological function or neuroimaging indicators after MSC transplantation, with no adverse effects reported.[22,23] Given the safety and potential efficacy of MSC transplantation, whether its combination with TMS may confer superior benefits for stroke treatment warrants in-depth investigation.[24,25] Indeed, donor MSCs do not persist long-term in the organ parenchyma and are gradually cleared by the host over time.[26] It could be hypothesized that iTBS may prolong the retention of MSCs to provide a critical therapeutic window, allowing sufficient time for triggering endogenous repair, such as the activation of endogenous NSCs and neurogenesis. However, evidence from preclinical studies, particularly those involving large animals, remains insufficient to prove this point.

Nonhuman primates (NHPs) are highly similar to humans in terms of genetics, neuroanatomy, physiology, immunology, and, in particular, pathology and pathophysiology changes following stroke, meaning that positive findings from even a small cohort carry significant translational weight.[27,28] In the present study, we established a left middle cerebral artery occlusion (MCAO) model in *Macaca fascicularis* to investigate the therapeutic potential of a combined intervention of MSC transplantation and TMS for chronic stroke (2 years after model induction) treatment. In addition, the underlying mechanisms mediating the therapeutic benefits were also studied via a battery of tests, including behavioral tests, electrophysiological recordings, functional magnetic resonance imaging (fMRI), magnetic resonance spectroscopy (MRS), plasma proteomic analysis, and terminal histological and spatial proteomic analysis. We sought to provide research evidence from NHP models to justify the possibility of future clinical use of the combined intervention of MSC transplantation and TMS.

RESULTS

Survival of donor MSCs in the MCAO monkey brain

One month after left middle cerebral artery occlusion surgery, 3D-TOF (time-of-flight) magnetic resonance angiography (MRA) was employed to assess the occurrence of middle cerebral artery occlusion in the monkey MCAO model. The results revealed the absence of vascular signals from the left middle cerebral artery and its branches on the affected side (Supplementary Fig. 1a). Two years after the establishment of the stroke model, we drilled 9 holes in the skull of the left cerebral hemisphere at predefined injection sites and delivered FITC-conjugated SPION-labeled MSCs into the surrounding area of the injury area and subventricular region through these perforations (Supplementary Fig. 1b, c). Transcranial iTBS magnetic stimulation was performed five times weekly, beginning one week after stem cell transplantation surgery, and the entire experiment lasted until the end of week 17 postsurgery (Supplementary Fig. 1d). Assessments were conducted at various time points before and after treatment, with the detailed specific measurements depicted in the gray box in the lower panel of Supplementary Fig. 1. All three MCAO monkeys (IDs: 11688, 11692, 11685) successfully recovered from the stem cell transplantation procedure, and no postoperative complications, such as cerebral hemorrhage or death, were observed. Monkeys 11688 and 11692 showed an uneventful recovery, regaining their preoperative general condition and dietary intake by the fifth postoperative day. Monkey 11685 experienced a transient neurological deficit characterized by mild weakness and a slower recovery of its general condition, particularly in alertness and activity levels, which began to improve by the seventh day and resolved completely by the end of the second week.

iTBS was applied one week after MSC transplantation and continued until the experimental endpoint at the 17th week. Serial MRI examinations were performed at baseline (1 week before transplantation) and at, refs. [1,5,9,13] and[17] weeks after transplantation to assess longitudinal changes in the brain condition and track the distribution of the transplanted cells (Fig. 1a). Prior to transplantation, the SPION-labeled stem cells emitting green fluorescence were observed via fluorescence microscopy (Fig. 1b, white arrows). The presence of iron nanoparticles within the cells was validated by Prussian blue staining, which revealed blue particle deposition in the cytoplasm (Fig. 1c, black arrows). Transmission electron microscopy revealed the presence of iron nanoparticles with typical high electron density in the cytoplasm (Fig. 1d, red arrows). These results confirmed that the MSCs were effectively labeled with FITC-conjugated SPIONs, allowing in vivo tracking of the transplanted stem cells. Before MSC transplantation, MRI-T2 imaging revealed homogeneous signals within the brain parenchyma of all monkeys. Postoperative MRI assessments conducted in the first week following surgery revealed the emergence of multiple distinct low-intensity regions at the injection sites in the brains of all monkeys that received MSC transplantation. As the transplanted cells were labeled with SPIONs, which typically manifest as regions of signal void or hypointensity on MRI due to their ability to decrease the signal density, the areas of low density indicated by the arrows

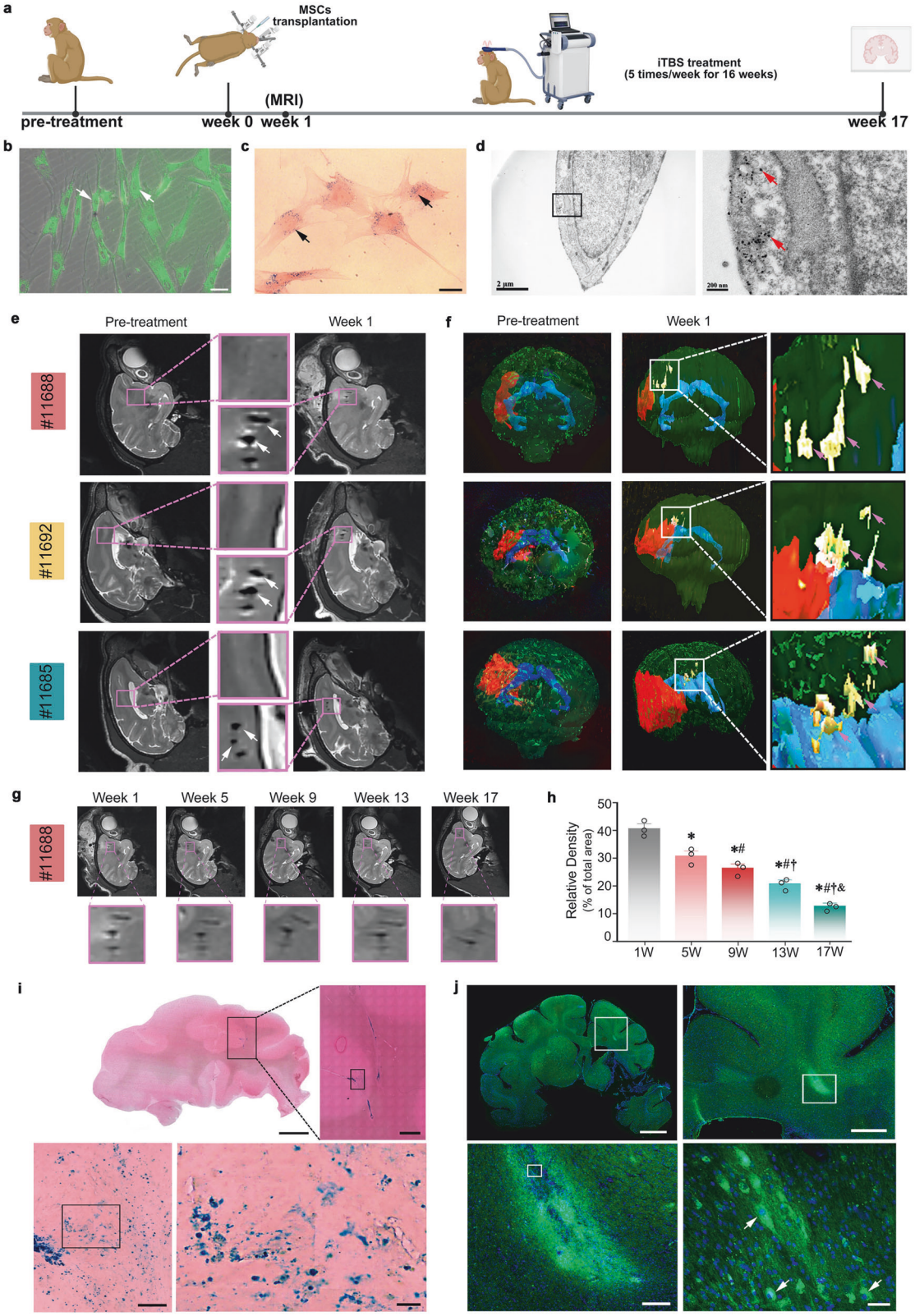

correspond to the distribution of the transplanted cells (Fig. 1e, white arrows). The spatial relationships among transplanted stem cells, cerebral ventricles, and infarcts were delineated through three-dimensional (3D) reconstruction of MR images, with the lateral ventricles being pseudocolored blue, the infarctions red, and the transplanted cell regions white, respectively. MRI imaging from the 1st week after surgery revealed that the transplanted MSCs were positioned in the area between the lesioned area and the lateral ventricles (Fig. 1f, pink arrows), which was in line with the transplantation plan, suggesting the success of stereotactic

Fig. 1 Brain MRI and 3D reconstruction, Prussian blue staining and fluorescence microscopic imaging of brain sections. **a** Timeline diagram of MRI and morphological detection. **b** MSCs labeled with FITC-conjugated SPIONs exhibit green fluorescence under a fluorescence microscope. **c** Prussian blue staining reveals extensive blue particle deposition within cells (black arrows). **d** Transmission electron microscopy reveals the presence of iron nanoparticles inside cells (iii, red arrows). **e** MR images of three monkeys before and after cell transplantation surgery. The left panel shows the pretransplantation MR images, whereas the right panel shows the posttransplantation MR images. High-magnification images are highlighted within a pink box, and the hypodense areas are indicated by arrows. **f** Three-dimensional (3D) brain reconstructions of three monkeys before and after cell transplantation surgery. The infarcted injury area is denoted in red, the lateral ventricles are denoted in blue, and the stem cells transplanted are denoted in white. The region enclosed by the box is magnified, with arrows indicating the area of stem cell transplantation (pink arrows). **g** Representative MR images of hypo-intense signals representing transplanted stem cells in the monkey brain at weeks 1, 5, 9, 13, and 17 after stem cell transplantation. **h** Bar chart showing the quantification results of hypo-intense signals at various time points throughout the study (* $p < 0.05$ vs. week 1; # vs. week 5; † vs. week 9; & vs. week 13, $n = 3$). **i** Panoramic view of a Prussian blue-stained monkey brain section (light microscopy). Successively higher-magnification images of areas boxed reveal Prussian blue-positive MSCs. **j** Panoramic view of a monkey's brain under a fluorescence microscope. The boxed region is then shown at progressively higher magnifications, revealing the fine details of the green fluorescent MSCs. Scale bars = 20 μm in (**b, c**); 5 mm in the upper-left images of (**i, j**); 1 mm in the upper-right images of (**i, j**); 200 μm in the lower-left images of (**i**, **j**); 40 μm in the lower-right image of (**i**); and 20 μm in the lower-right image of (**j**)

injection. MRI imaging at 1, 5, 9, 13, and 17 weeks post-surgery revealed that the hypo-intense signals in the brains of the three monkeys gradually diminished over the four months, with hypointense shadows still present by the 17th week (Fig. 1g, h; Supplementary Fig. 2). Notably, for animal 11,685, the signal became exceedingly faint by the 17th week. This situation determines the time point for the acquisition of brain tissue for subsequent morphological analysis for donor function.

Prussian blue staining revealed multiple blue areas in the hemispheres of the injury/graft side at low magnification and several blue-stained cells in each cell cluster at high magnification. A close look suggested that these cells presented large cell bodies with two to several cell processes. These findings suggest that these cells contain a significant amount of iron nanoparticles, indicating the presence of donor cells (Fig. 1i). Additionally, many green fluorescent cells were also observed in the brain sections on the injury/graft side via fluorescence microscopy (Fig. 1j, Supplementary Fig. 3). Taken together, these results suggested the survival of donor cells for up to 17 weeks in the brains of all three monkeys. Therefore, the paradigm to detect the viability of transplanted MSCs within the monkey brain through MRI data, Prussian blue staining of monkey brain tissue, and the morphological presence of green fluorescent cells was proven to be effective.

Improvement in upper limb motor function recovery and metabolic alterations in the sensorimotor cortex

To evaluate the therapeutic benefits of MSC transplantation combined with iTBS on upper limb motor deficits in monkeys following chronic stroke, we performed a series of behavioral assessments at 6 months, 5 months, and 1 week before transplantation, followed by further evaluations at 5, 9, 13, and 17 weeks after transplantation. The behavioral assessment included scores and completion times for both left and right upper limb performance on the hill staircase task and the valley staircase task. Additionally, the assessment included the utilization rate and completion time of the affected upper limb (right hand) in performing the object retrieval task.

The baseline data revealed a plateau in the upper limb motor function score of the affected upper limb from 6 months to 1 week prior to cell transplantation. A slight decline in motor function score was noted in the contralateral upper limb (Fig. 2a, b). Similarly, no significant changes in completion time in the hillside staircase task were observed in the affected upper limb before cell transplantation, whereas there was an increase in the time needed for the contralateral upper limb to complete this task (Fig. 2a, b). Additionally, in the object retrieval task, there was no significant change in the utilization rate or completion time of the affected upper limb (Fig. 2c). Furthermore, in the valley staircase task, the performance score of the affected upper limb decreased, whereas that of the contralateral upper limb remained unchanged (Fig. 2d). The time required to complete this task was increased for both sides of the limbs (Fig. 2d).

Compared with pretransplantation at baseline (1 week prior to cell transplantation), the combination of intraparenchymal MSC transplantation and iTBS resulted in a measurable increase in the upper limb motor function of monkeys with chronic stroke. The results of the hill staircase task revealed that the scores for the affected upper limbs partially improved at week 9 posttransplantation compared with those at the prior time point (week 5 posttransplantation), with no further increases at weeks 13 or 17. The scores of the hill staircase task for the contralateral upper limbs decreased at week 9 posttransplantation, returned to baseline levels by week 13, and maintained this trend through week 17 (Fig. 2e, f). There was no significant change in the hill staircase task completion time for the affected upper limb, whereas the completion time for the contralateral upper limb decreased continuously (Fig. 2e, f). In the object retrieval task, a measurable increase in the success rate of the affected upper limb was observed, and the task completion time decreased significantly (Fig. 2g). In the valley staircase task, the scores for the affected upper limbs increased to a limited extent, whereas the scores for the contralateral limb remained unchanged (Fig. 2h). There was no significant alteration in the completion time of the affected upper limb in the valley staircase task; however, the completion time of the contralateral upper limb was significantly reduced (Fig. 2h). Representative behavioral videos before and after treatment are provided in the supplementary materials (Supplementary Videos 1–3).

Magnetic resonance spectroscopy (MRS) leverages the magnetic resonance chemical shift to identify and quantify the molecular constituents of biological tissues, allowing a preliminary assessment of metabolite levels within the bilateral sensorimotor cortex (SMC) (the orange area in Fig. 2i). In this exploratory analysis, we captured metabolic changes at multiple time points before and after treatment, including the concentrations of total N-acetylaspartate (tNAA), total choline (tCho), microtubule-associated protein tau (Tau), and phosphocholine (PCh), which are pivotal for neural injury repair. The MRS profiles of the left and right SMC regions demonstrated metabolic chemical shifts specific to this brain area. tNAA typically peaks at approximately 2.0 parts per million (ppm), tCho at nearly 3.2 ppm, and PCh at 3.2 ppm, closely resembling tCho, albeit with a marginally distinct peak shape. Additionally, the level of the tau protein, which is associated with microtubules, peaked at approximately 1.3 ppm (Fig. 2j, k). Statistical analysis revealed a significant increase in tNAA concentrations within the left SMC, with an initial increase from 7.39 ± 0.88 mmol/L before treatment to 11.32 ± 1.31 mmol/L one week post-treatment. A significant decline was observed immediately, with levels decreasing to 4.08 ± 0.83 mmol/L at week

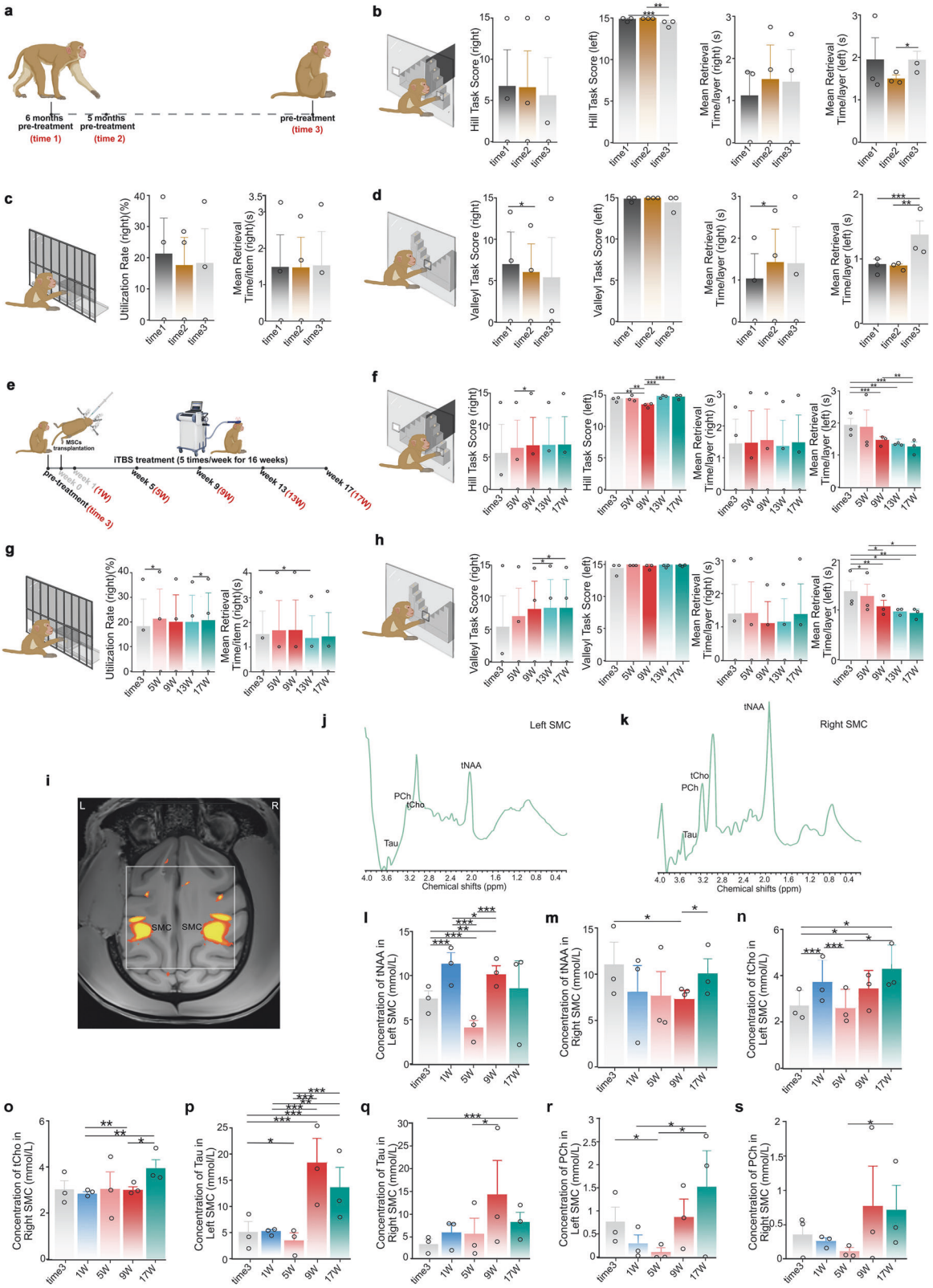

5. By the ninth week, tNAA levels had rebounded to match the first week post-treatment values at 10.10 ± 1.01 mmol/L, and by the seventeenth week, despite a slight decrease to 8.5 ± 3.14 mmol/L, they remained elevated compared with pre-treatment levels. The analysis of the tNAA concentration in the right SMC region revealed different patterns. Initially, the tNAA concentration tended to decrease, but at the 17th week after treatment, it had recovered to the same level as before treatment; that is, the concentration of tNAA on the noninjured side did not change significantly (Fig. 2i, m). Statistical analysis revealed

Fig. 2 Effects of MSC transplantation and transcranial iTBS on motor function and metabolites in the sensorimotor cortex (SMC) in monkeys with chronic stroke. **a** Schematic diagram of pretreatment behavior assessment time points for MCAO stroke monkeys. **b** This panel consists of a schematic diagram of the hill staircase task and four bar graphs depicting pretreatment performance (scores for each upper limb and bilateral completion time) at 6 months, 5 months, and 1 week. **c** Schematic diagram of the object retrieval task, along with two bar graphs showing the pretreatment utilization rate of the affected upper limb and the task completion time at 6 months, 5 months, and 1 week. **d** Schematic diagram of the valley staircase task. The four bar graphs show the pretreatment scores for the right and left upper limbs and the task completion times for both limbs at 6 months, 5 months, and 1 week. **e** Time point diagram of behavior assessment in MCAO stroke monkeys after treatment. **f** Schematic diagram of the hill staircase task. Accompanying bar graphs show the scores for the right and left upper limbs and the task completion times at 1 week before treatment and at 5, 9, 13, and 17 weeks after treatment. **g** Schematic diagram of the object retrieval task, with accompanying line graphs showing the utilization rate of the affected upper limb and the task completion time at 1 week before treatment and at 5, 9, 13, and 17 weeks after treatment initiation. **h** Schematic diagram of the valley staircase task. The four accompanying graphs show the scores and the task completion times for the right and left upper limbs, respectively, from 1 week before treatment to 17 weeks after treatment initiation. **i** MRI of the monkey brain, with the orange areas highlighting the SMC regions on both the left and right hemispheres. **j**, **k** MRS spectra of the left and right SMCs, illustrating the characteristic peaks for tNAA, tCho, Tau, and PCh across their respective chemical shifts. **l**–**o** Serial quantification of tNAA, tCho, Tau, and PCh levels in the left SMC across five time points: pretreatment at baseline and week 1, week 5, week 9, and week 17 posttreatment. **p**–**s** Quantified levels of tNAA, tCho, Tau, and PCh in the right SMC. Bars represent measurements at pretreatment baseline and at 1, 5, 9, and 17 weeks post-treatment (*$p < 0.05$, **$p < 0.01$, *** $p < 0.001$; $n = 3$)

dynamic tCho changes in the bilateral SMC: the left SMC concentration increased from 2.70 ± 0.38 mmol/L (pretreatment) to 3.72 ± 0.56 mmol/L at 1 week post-treatment, decreased to 2.58 ± 0.48 mmol/L by week 5, and then increased to 4.29 ± 0.60 mmol/L by week 17 ($p < 0.05$ vs. baseline). Similarly, the right SMC showed parallel trends—elevating at 1 week, decreasing by week 5, and peaking at 3.98 ± 0.38 mmol/L by week 17 ($p < 0.05$ vs. pretreatment 3.06 ± 0.38 mmol/L), with both hemispheres exhibiting an increasing trend in the late phase (Fig. 2n, o). Tau concentrations in bilateral SMCs exhibited parallel dynamics: minimal fluctuations occurred at pretreatment and at 1 and 5 weeks post-treatment, followed by a significant increase at week 9 ($p < 0.001$). Despite a modest decline by week 17, the levels remained substantially elevated compared with those at baseline in both the left (13.66 ± 3.80 vs. 5.11 ± 2.00 mmol/L) and right (8.29 ± 2.14 vs. 3.4 ± 1.13 mmol/L; $p < 0.001$) SMCs (Fig. 2p, q). The trend of Pch concentration was also similar on the left and right sides, with a decrease observed at the initial three time points: pretreatment, one week post-treatment, and five weeks post-treatment. PCh concentrations continued to increase on the left side by the seventeenth week post-treatment, whereas concentrations on the right side stabilized at the levels observed at the ninth week. Compared with the pretreatment measurements, both sides presented significantly elevated levels (left side: 1.52 ± 0.78 mmol/L compared with 0.77 ± 0.32 mmol/L; right side: 0.72 ± 0.36 mmol/L compared with 0.36 ± 0.18 mmol/L, $p < 0.05$; Fig. 2r, s). Taken together, the longitudinal MRS data revealed dynamic fluctuations in key metabolites but demonstrated an overall positive trend relative to preintervention levels.

We further analyzed fluctuations in the concentrations of multiple metabolites in the stem cell injection site area (ISA, highlighted by the orange region in Supplementary Fig. 4a). This assessment included the quantification of aspartic acid (Asp), lactate (Lac), glutamine (Gln), gamma-aminobutyric acid (GABA), Glucosae (Glc), inositol (Ins), and glycerophosphocholine (GPC) contents. The spectrogram showed characteristic peaks for several metabolites: Asp typically peaked between 2.2 and 2.5 ppm, Lac at approximately 1.3 ppm, Gln at approximately 2.1 ppm, GABA at approximately 1.9 ppm, and Glc at approximately 4.7 ppm. Additionally, Ins was observed between 3.3 and 3.4 ppm, and GPC was observed at approximately 3.2 ppm (as depicted in Supplementary Fig. 4b). The results revealed that the Asp concentration within the ISA increased from a pretreatment level of 49.52 ± 10.55 mmol/L to 72.43 ± 27.64 mmol/L one week post-treatment, with this concentration being sustained through the seventeenth week of the study (Supplementary Fig. 4c). Lactate (Lac) levels exhibited an inverse trend, beginning at 18.23 ± 12.18 mmol/L pretreatment and declining to 3.26 ± 0.64 mmol/L one week after treatment (Supplementary Fig. 4d). The GABA concentration slightly increased one week after treatment, with a continuous increasing trend observed at the 5th and 9th weeks. By the 17th week, the GABA levels stabilized and remained relatively high compared with the values measured before treatment (Supplementary Fig. 4e). However, differences in these four metabolites, including Asp, Lac, and GABA, did not reach statistical significance. The concentration of Glc in the ISA significantly changed from a pretreatment level of 8.47 ± 2.78 mmol/L to 14.47 ± 4.08 mmol/L at the 17th week after treatment ($p < 0.001$, Supplementary Fig. 4f). The changes in Ins and GPC at the ISA were similar to those of Glc, with notable increases in concentration during the initial week post-treatment, a decrease in the 5th week, and a slight increase in the 9th and 17th weeks. Despite these fluctuations, the levels of Ins and GPC remained relatively elevated relative to pretreatment measurements. However, these differences did not reach statistical significance (Supplementary Fig. 4g, h). We also evaluated changes in the Gln concentration between the ISA and the contralateral symmetric area (CSA). The results revealed that the Gln concentrations on both sides increased from the 1st week post-administration, with similar levels observed. The ISA side reached its peak at the 9th week and declined by the 17th week but remained higher than the pretreatment levels. In contrast, the Gln concentrations on the CSA side began to decrease from the 5th week and continued to decrease to pretreatment levels (Supplementary Fig. 4i). However, the changes in Gln did not reach statistical significance.

The above results indicated that after receiving the MSC transplantation combined with iTBS regimen, all monkeys showed improvements in behavioral scores, reduced task completion times, and increased success in the tested tasks. Moreover, this treatment strategy affected metabolite levels in the SMC and ISA areas of chronic stroke monkeys.

Increased cortical excitability and nerve conduction velocity

Electrophysiological assessments of cortical excitability and nerve conduction velocity were conducted to measure alterations in the resting motor threshold (RMT) and latency both before and after transplantation. The RMT reflects the excitability of corticospinal projections during relaxation and is conventionally defined as the minimum stimulation intensity necessary to consistently elicit an MEP of at least 50 microvolts (μV) in at least half of the tests.[29] For monkey 11688, both hemispheres were capable of eliciting motor evoked potentials (MEPs), with a pretransplantation resting motor threshold (RMT) at 50% of the maximum stimulator output (MSO). Following the combined therapy, there was a noticeable trend toward a reduction in RMT in both hemispheres. Notably, the left

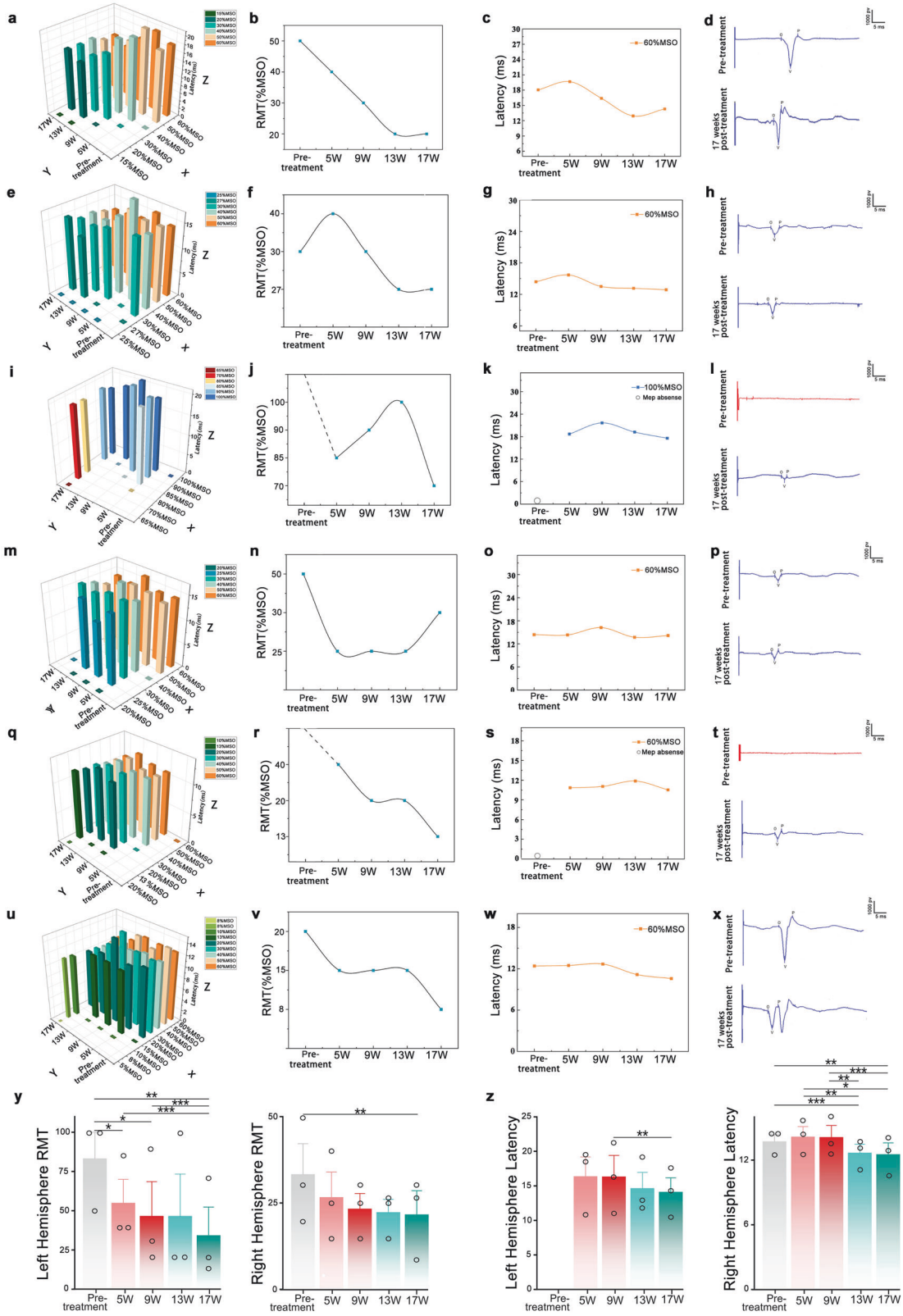

hemisphere (injury side) exhibited a more pronounced decrease, with the RMT decreasing from 50% to 20% of the MSO at the final assessment point at the 17th week post-transplantation (Fig. 3a, b). The latency was assessed via 60% MSO, and the results indicated a reduction in the latency of evoked MEPs in the left hemisphere following the combined therapy (Fig. 3c, d). In the right hemisphere, the RMT decreased from 30% to 27% of the MSO (Fig. 3e, f), and the MEP latency also decreased (Fig. 3g, h).

For monkeys 11692 and 11685, MEPs could not be elicited even at 100% MSO in the injured hemisphere before treatment.

Fig. 3 Electrophysiological improvement in chronic stroke monkeys after combination therapy with stem cell transplantation and iTBS. **a**, **e** Three-dimensional histograms depicting the relationships among time points, RMT, and latency in the left and right hemispheres of monkey ID 11688, respectively. The X-axis corresponds to the time point, the Y-axis corresponds to the RMT, and the Z-axis corresponds to latency. The intensity levels of stimulation (% of MSO) are indicated by different colors, with color intensity correlating with stimulus intensity. Notably, data points represented solely by color without corresponding bar heights indicate instances where MSO of the specified intensity was applied but failed to elicit MEP. **b**, **f** Variations in RMT at each time point before and after treatment on the left and right sides, respectively. **c**, **g** The latency change curves plotted at each time point on the left and right sides, respectively. **d**, **h** Representative images of MEP waveforms captured at the initial time point (1 week prior to treatment) and at the final time point (17 weeks post-treatment) on the left and right sides, respectively. **i**, **m** Three-dimensional histograms of the time point, RMT, and latency within the left and right hemispheres of subject monkey ID 11692, respectively. **j**, **n** RMT changes at each time point before and after treatment for monkey ID 11692. **k**, **o** Latency changes in the left and right hemispheres over time in monkey ID 11692. **l**, **p** Representative images of MEP waveforms for monkey ID 11692 captured at 1 week prior to treatment and 17 weeks post-treatment. **q**, **u** Three-dimensional histograms of the time point, RMT, and latency within the left and right hemispheres of monkey ID 11685, respectively. **r**, **v** RMT changes at each time point before and after treatment for monkey ID 11685. **s**, **w** Latency of the left and right hemispheres over time for monkey ID 11685. **t**, **x** Representative images of MEP waveforms for monkey ID 11685 on the left and right sides, respectively. **y** Statistical plots displaying RMT at various time points in both the left and right hemispheres of all monkeys. **z** Statistical plots of latency at each time point in both the left and right hemispheres of all monkeys. (*$p < 0.05$, **$p < 0.01$, ***$p < 0.001$; $n = 3$)

However, by week 5 posttreatment, MEPs could be evoked at 85% or 40% MSO for 11692 and 11685, respectively (Fig. 3i–l; q–t). At the final assessment time point (the 17th week), the RMT of the left hemisphere had decreased to 70% or 13% for 11692 and 11685, respectively (Fig. 3j, r). Owing to the failure to induce MEPs, latency was not detected in the injured hemisphere at 1 week before treatment for either 11692 or 11685 (highlighted in red, Fig. 3l, t). MEP induction was successfully achieved in the lesioned cerebral hemisphere at 5 weeks post-treatment for 11692, with an initial latency of 19.34 milliseconds (ms). The latency was subsequently reduced to 17.56 ms following 17 weeks of treatment for 11692 (Fig. 3k, l). However, there was a mild change in the latency of the left hemisphere for 11685 at subsequent time points (Fig. 3s). In the contralateral hemisphere, the RMT also decreased from 50% to 30% or 20% to 8% of the MSO for 11692 and 11685, respectively (Fig. 3m, n; u, v). The latency also decreased from 14.50 ms to 14.16 ms or 12.36 ms to 10.98 ms for 11692 and 11685, respectively (Fig. 3o, p; w, x).

Data from three monkeys, including RMT and latency values for both the injured and contralateral hemispheres, were subjected to statistical analysis. The results revealed a statistically significant reduction in the RMT of the injured hemisphere from one week prior to treatment to all posttreatment time points assessed (the 5th, 9th, 13th, and 17th weeks; Fig. 3y, left panel). On the contralateral side, the analysis revealed that the decrease in RMT was statistically significant between the 1st week before transplantation and 17 weeks after transplantation (Fig. 3y, right panel). The latency analysis revealed a statistically significant reduction in latency on the injured side between the 9th week and the 17th week post-transplantation (Fig. 3z, left panel). On the contralateral side, latency was significantly reduced at weeks 13 and 17 posttransplantation relative to that at the prior three time points (Fig. 3z, right panel). The above results revealed that, in monkeys, the treatment resulted in a better electrophysiological presentation characterized by a decreased RMT and a shortened latency.

Enhancement in brain activity intensity, neuronal activity consistency, and brain functional connectivity

To explore the mechanisms underlying the motor function recovery and electrophysiological improvements associated with the treatment, functional magnetic resonance imaging (fMRI) was utilized to assess alterations in neural activity intensity, neural activity synchronization, and brain functional connectivity within the cerebral cortex of monkeys before and after transplantation. Regional neural activity intensity was quantified via Amplitude of Low-Frequency Fluctuations (ALFF), which denotes the aggregate power of the BOLD (Blood Oxygen Level Dependent) signal within the low-frequency bandwidth of 0.01--0.1 Hz. The results indicated a posttreatment enhancement of neural activity within the primary motor cortex, as reflected by an intensified ALFF (red hotspot in Fig. 4a) in the corresponding region. The ALFF values were standardized via the z score method to obtain zALFF values, reducing interindividual physiological variability and enhancing the comparability of the results. Statistical analysis of the zALFF values in the left primary motor cortex of three monkeys across various time points posttreatment revealed alterations. Initially, the zALFF value was 0.32 ± 0.11 in the first week prior to treatment. This value increased to 0.59 ± 0.28 in the first week after treatment. However, a decrease was observed in the fifth week, with the zALFF value decreasing to 0.42 ± 0.39. The zALFF value subsequently increased again, reaching 0.69 ± 0.42 by the ninth week post-treatment, and further increased to 1.00 ± 0.43 by the seventeenth week. Notably, the changes observed at these three time points were statistically significant, indicating a progressive increase in neural activity in the left primary motor cortex following treatment (Fig. 4f, left panel). In the right primary motor cortex, the zALFF values exhibited minimal variation, with a pretreatment mean of 0.42 ± 0.37, which marginally increased to a mean of 0.54 ± 0.16 by the 17th week post-treatment. No statistically significant difference was found in the values of each timepoint group during this time, suggesting little change in right-sided nerve activity (Fig. 4f, right panel).

Neural activity synchronization was assessed via Regional Homogeneity (ReHo), which quantifies the temporal similarity of BOLD signal time series within a voxel and its surrounding voxels, thereby reflecting the coherence of neural activity across brain regions. Detection results at various time points before and after treatment revealed an increase in neural activity synchronicity within the primary motor cortex following the combination therapy, as indicated by an increased ReHo value (as shown by the red hot spot in Fig. 4b) in the pertinent region. Consistently, the z score standardization method was also applied to normalize the ReHo values, resulting in zReHo, which then facilitated subsequent statistical analyses. Statistical analysis of the zReHo values in the left primary motor cortex revealed a significant upward trend. Prior to treatment, the mean zReHo value was 0.51 ± 0.08. This value rose to 0.73 ± 0.18 in the first week after treatment, indicating an early response to the therapeutic intervention. The increase continued to 0.76 ± 0.33 by the fifth week post-treatment and further increased to 0.93 ± 0.27 by the ninth week. The most substantial increase was observed at the seventeenth week, when the zReHo value reached 1.28 ± 0.37. The statistical significance of these changes was evident when the ReHo values from one week prior to treatment were compared with those at five, nine, and seventeen weeks post-treatment (Fig. 4g, left panel). On the right side, similar to the zALFF value, the zReHo value exhibited a modest increase, starting at 0.41 ± 0.24 before the intervention and increasing to 0.56 ± 0.24

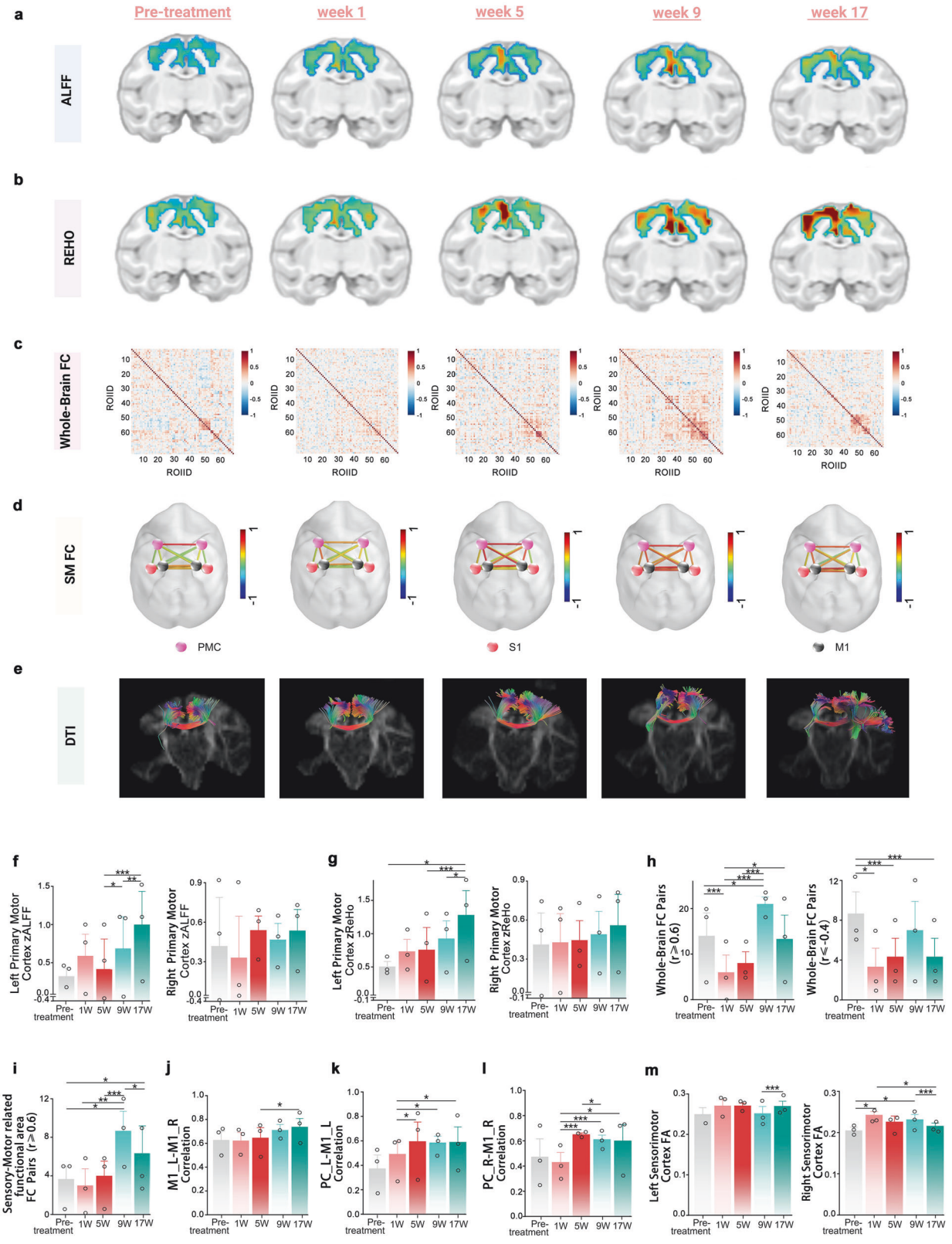

by the seventeenth week post-treatment. Despite this slight upward trend, no statistically significant differences were detected among these groups (Fig. 4g, right panel).

The functional connectivity of the whole brain was assessed by examining the correlation strength between various brain regions. By utilizing a correlation matrix—a visual representation that maps the functional connectivity patterns—our analysis revealed distinct changes in these patterns. Typically, a red color indicates a positive correlation, suggesting that the activities of the two brain regions rise or fall in concert. Conversely, blue signifies a negative

Fig. 4 fMRI and DTI analyses of chronic stroke monkeys at multiple time points before and after combined therapy intervention. **a** ALFF images of the primary motor cortex at pretreatment (1 week before treatment), week 1 (one week post-transplant surgery), week 5 (five weeks post-transplant surgery), week 9 (nine weeks post-transplant surgery), and week 17 (seventeen weeks post-transplant surgery). **f** Bar chart showing the quantification results of ALFF in the left and right primary motor cortex. **b** ReHo images of the primary motor cortex at pretreatment, week 1, week 5, week 9, and week 17. **g** Bar chart displaying the quantification results of ReHo in the left and right primary motor cortex. **c** Correlation matrix plot of the primary motor cortex at the five time points demonstrating changes in both positive and negative whole-brain functional connectivity (FC). **h** Bar chart showing the quantification results of positive whole-brain FC pairs ($r \geq 0.6$) and negative whole-brain FC pairs ($r \leq -0.4$). **d** Brain network map showing changes in functional connectivity (FC) strength in the S1, M1, and PMC regions of the left and right hemispheres at 5 time points. **i** Bar chart displaying the quantification results of sensory-motor-related functional area-positive FC pairs. **j** Bar chart displaying the quantification results of the correlation between the left and right M1 regions. **k** Bar chart displaying the quantification results of the correlation between the left PMC and M1 regions. **l** Bar chart displaying the quantification results of the correlation between the right PMC and M1 regions. **e** DTI tractography visualization of nerve fiber bundles in the sensorimotor cortex. **m** Bar chart displaying the quantification results of FA in the left and right sensorimotor cortices. (*$p < 0.05$, **$p < 0.01$, ***$p < 0.001$; $n = 3$)

correlation, where an increase in activity in one region is associated with a decrease in the other (Fig. 4c). Statistical evaluation of the correlation strength among 70 gray matter regions (listed in Supplementary Table 2) at multiple time intervals before and after treatment revealed a dynamic shift in connectivity. Posttreatment, there was an initial decline in positive correlation ($r \geq 0.6$) during the first week, followed by a marked increase at both the fifth and ninth weeks. This was succeeded by a subsequent decrease by the seventeenth week (Fig. 4h, left panel). In contrast, negative correlations ($r \leq -0.4$) experienced a significant decrease in the first week, a slight rebound at the fifth and ninth weeks, and a persistent decline by the seventeenth week (Fig. 4h, right panel).

The functional connectivity within the sensorimotor (SM) brain region, encompassing the primary somatosensory cortex (S1), primary motor cortex (M1), and premotor cortex (PMC) in both hemispheres, was evaluated by analyzing the correlation strength among these areas (Fig. 4d). Each node corresponds to S1, M1, and PMC in both the left and right hemispheres of the brain. The lines interconnecting these nodes denote the functional linkages between these regions. The color gradient of these lines signifies the magnitude of connectivity, with redder hues indicating stronger connections and bluer tones suggesting weaker connections. Statistical analysis of the functional connectivity within sensory-motor-related regions at various time points before and after treatment revealed no significant alterations from pretreatment levels through the fifth week post-treatment. A notable increase in connectivity was observed at the ninth week. Although a decrease was noted at the seventeenth week, connectivity levels remained elevated compared with those at the pretreatment baseline (3.67 ± 1.33 vs. 6.33 ± 2.85, $n = 3$). There were significant differences in these changes ($p < 0.05$; Fig. 4i). The functional connectivity between the left and right M1 regions exhibited a modest trend toward enhancement. Specifically, the measure increased from a pretreatment value of 0.63 ± 0.07 to 0.74 ± 0.07 by the seventeenth week post-treatment. Notably, the statistical analysis revealed significant differences in functional connectivity between the fifth week and the seventeenth week after treatment ($p < 0.05$; Fig. 4j). The functional connectivity between the left PMC region and the ipsilateral M1 revealed an increasing trend, with a pretreatment connectivity measure of 0.37 ± 0.11, which increased to 0.59 ± 0.12 by the seventeenth week post-treatment. Significant differences were observed when the connectivity at one week post-treatment was compared with that at weeks five, nine, and seventeen, suggesting a progressive strengthening in the functional linkage between these regions over the treatment duration ($p < 0.05$; Fig. 4k). The functional connectivity between the right premotor cortex (PMC) and primary motor cortex (M1) significantly increased from 0.47 ± 0.14 before treatment to 0.60 ± 0.13 at week 17 after treatment. Statistically significant differences were observed when week 1 was compared with weeks 5, 9, and 17, indicating robust enhancement in connectivity over time ($p < 0.05$; Fig. 4l).

In addition to fMRI, diffusion tensor imaging (DTI) was employed to monitor and visualize neural fiber tracts within the brain, thereby evaluating the impact of the combined therapeutic approach on white matter fiber restoration in chronic stroke monkeys. The depicted colored lines correspond to neural fiber bundles, with their density and continuity indicative of the structural integrity and connectivity of white matter. Traditionally, red denotes the anterior–posterior orientation, green signifies the left–right trajectory, and blue represents the superior–inferior direction (Fig. 4e). Fractional anisotropy (FA) values were calculated via DSI-Studio software to analyze the DTI scans. As a quantitative measure of white matter tract integrity, FA values increase with greater directional consistency, which is indicative of more efficient neural transmission. The results indicate a modest increase in FA values within the left sensorimotor cortex over the course of treatment, transitioning from a pretreatment value of 0.25 ± 0.02 to 0.27 ± 0.01 by the seventeenth week post-treatment. A statistically significant difference was observed between the FA values at week 9 and week 17 posttreatment ($p < 0.001$; Fig. 4m, left panel). The FA value in the right sensorimotor area also slightly increased, increasing from a pretreatment value of 0.21 ± 0.01 to 0.24 ± 0.01 in the initial week following treatment, with this increase being statistically significant. Subsequently, there was a minor reduction, with the FA value decreasing to 0.22 ± 0.01 by the seventeenth week post-treatment but remaining marginally above the baseline level (Fig. 4m, right panel).

These findings indicate that the synergistic application of MSC transplantation and iTBS enhances neural activity intensity, neural synchronization, and positive functional connectivity within the sensorimotor cortex in chronic stroke monkeys. Additionally, this combined therapy augments the directional coherence of white matter tracts, which is conducive to more efficient neural conduction.

Plasma proteomics and brain spatial proteomics reveal the activation of neurogenesis and chemotaxis signaling after treatment

Plasma samples were collected from the monkeys one week before and 17 weeks after treatment. These samples were subjected to comprehensive proteomic analysis to assess changes in the protein expression profile induced by the treatment. Compared with pretreatment levels, a total of 50 differentially expressed proteins were identified (Supplementary Fig. 5a). Hierarchical clustering heatmap analysis of the differentially expressed proteins revealed that the treatment significantly upregulated plasma proteins associated with neural activation, synaptic formation, anti-inflammation and immunomodulation. Quantitative analysis revealed notable upregulation of proteins associated with neural activation and synaptic formation (Reelin, Coronin-1A, and Fibulin 5), cytokine and adhesion molecules

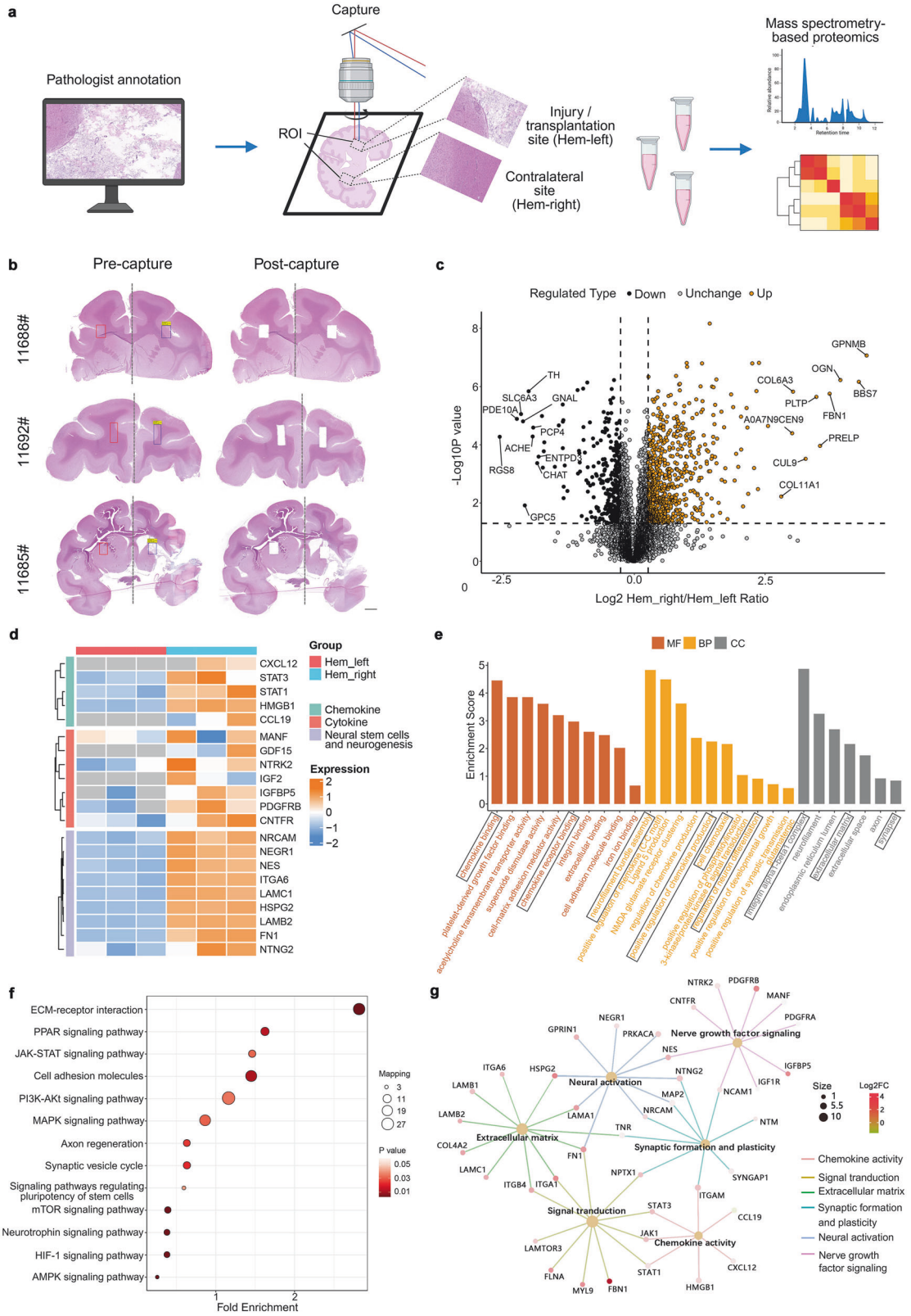

(insulin-like growth factor I, leucine-rich alpha-2-glycoprotein 1, and beta-2-microglobulin), and anti-inflammatory and immunomodulatory proteins (granulin precursor, protein S100 A9, and grancalcin) after treatment (Supplementary Fig. 5b, c). Furthermore, Kyoto Encyclopedia of Genes and Genomes (KEGG) pathway enrichment analysis of the differentially expressed proteins revealed that combination therapy triggered the activation of several signaling cascades related to neural activation and regeneration. These included pathways related to the IL-17 signaling pathway, pluripotency of stem cells, the AMPK signaling

Fig. 5 Pathways activated by neurogenesis and chemotaxis in the posttreatment brain identified by spatial proteomic profiling. **a** Schematic diagram of the spatial proteomics workflow. Specific regions of interest (ROIs) were microdissected from the ipsilateral injury/transplantation site (left hemisphere) and the contralateral uninjured symmetrical site (right hemisphere). These ROIs were defined as the parenchyma surrounding the MSC transplantation sites and the chronic infarct area. **b** H&E-stained brain sections from all three monkeys before and after microdissection, illustrating the precise areas of tissue microdissection. **c** Volcano plot depicting differentially expressed proteins in the ipsilateral injury/transplantation site group compared with the contralateral control group. Proteins are color-coded as follows: significantly upregulated (orange), significantly downregulated (black), and nonsignificant (gray). **d** Hierarchical clustering heatmap displaying the expression patterns of differentially expressed proteins related to chemotaxis, cytokine signaling, neural stem cells and neurogenesis. Relative protein expression is color-coded: orange indicates upregulation, and blue indicates downregulation. The rows represent individual proteins, and the columns represent the microdissected tissue samples from the left and right hemispheres. **e** Bar chart of the results of the GO enrichment analysis. Differentially expressed proteins related to chemotaxis and neurogenesis were significantly enriched. Representative terms from each ontology are shown: molecular function (MF, magenta), biological process (BP, orange), and cellular component (CC, gray). **f** KEGG pathway enrichment analysis of differentially expressed proteins. The bubble color intensity represents the statistical significance (*P*-value), whereas the bubble size corresponds to the number of proteins mapped to each pathway. **g** PPI network of enriched functional sets. Six significantly enriched functional sets were constructed, with their node sizes scaled to the number of member proteins. Individual proteins (nodes) are mapped between sets and colored by their log_2FC to visualize expression changes. Scale bar = 5 mm in (**b**)

cascade, the Ras signaling axis, the MAPK signaling route, and the PI3K–Akt pathway, among others (Supplementary Fig. 5d). Gene Ontology (GO) enrichment analysis indicated that combination therapy significantly altered the proteomic profile across key functional categories. Specifically, we observed significant enrichment in molecular functions (MFs) related to chemokine activity, biological processes (BP) governing nerve growth factor signaling and neuronal differentiation, and cellular components (CCs) comprising synaptic and axonal structures (shown in gray boxes in Supplementary Fig. 5e). Protein interaction network analysis revealed that the differentially expressed proteins were predominantly associated with neurotrophic signaling, neuronal survival, nerve regeneration, cytokine activity, anti-inflammatory and immune regulatory processes, synaptic formation and plasticity, and signal transduction. Furthermore, these proteins exhibited significant interactions with one another, indicating complex interplay in the biological network (Supplementary Fig. 5f). Plasma proteomic analysis revealed a significantly altered protein expression profile after treatment. In addition to mechanisms commonly attributed to MSCs—including cytokine secretion, anti-inflammatory activity, and immune modulation—the changes involved pathways associated with neurogenesis and chemotaxis.

Spatial proteomic analysis of brain tissue sections was performed to investigate the mechanisms underlying molecular changes following the combined treatment directly. Specifically, defined tissue regions were microdissected from both the ipsilateral injury/transplantation site in the left hemisphere and the contralateral uninjured symmetric site in the right hemisphere of each animal for mass spectrometry-based proteomic sequencing (Fig. 5a). H&E staining confirmed the tissue morphology and precise resection areas (Left/blue box: injury/transplantation site; Right/red box: contralateral control site; 11688: 9.9 mm^2, 11692: 9.6 mm^2, 11685: 9.9 mm^2; Fig. 5b). Proteomic comparison of the left hemisphere injury/transplantation site against the contralateral control site revealed substantial alterations, revealing 788 significantly upregulated and 321 downregulated proteins (Fig. 5c). Hierarchical clustering of these differentially expressed proteins revealed a distinct upregulation of proteins implicated in chemotaxis, cytokine signaling, neural stem cells, and neurogenesis (Fig. 5d). Consistent with the GO enrichment results from plasma proteomics, the differentially expressed proteins identified via spatial proteomics were significantly enriched in GO terms related to chemotaxis and neurogenesis. These included terms associated with MF terms such as chemokine binding and chemokine receptor binding; BP terms including neurofilament assembly, chemokine production, cell chemotaxis, and neuronal differentiation; and CC terms related to integrin complexes, the extracellular matrix, and synapses (as shown in the gray box in Fig. 5e). KEGG pathway analysis confirmed the activation of key signaling pathways previously suggested by plasma proteomics—such as the PI3K–Akt, MAPK, stem cell pluripotency, mTOR, and AMPK pathways—and uniquely revealed additional enrichment in extracellular matrix–receptor interactions, cell adhesion molecules, axon regeneration, the synaptic vesicle cycle, and neurotrophin signaling pathways (Fig. 5f). Finally, protein–protein interaction (PPI) network analysis revealed that these differentially expressed proteins were associated primarily with functional clusters of chemotactic activation, extracellular matrix organization, neural activation, synaptogenesis and plasticity and exhibited significant interconnectivity, indicating that a complex, coordinated molecular network underlies the treatment response (Fig. 5g).

Neural stem cell activation, chemotaxis, and neuronal differentiation

Histological analysis of brain sections was used to assess neurogenesis within the brain parenchyma following treatment. In a Nestin-immunofluorescent coronal section of the monkey brain (Fig. 6a), a central dashed line distinguishes the left (L, injury/transplantation site) and right (R, contralateral) hemispheres. Immunofluorescence staining revealed the absence of Nestin-positive cells in the right hemisphere of the monkey brain (Fig. 6b). In contrast, in the left hemisphere, which corresponds to the region of stroke injury and the site of MSC transplantation, a substantial number of Nestin-positive neural stem cells were observed (Fig. 6c). At higher magnification, Nestin-positive red fluorescence was localized to the cytoplasm, with the nuclei counterstained with the nuclear dye Hoechst (arrows, Fig. 6c). In the Musashi-1 immunofluorescence monkey brain coronal section, the central dashed line distinguishes the left (L) and right (R) hemispheres (Fig. 6d). On the right side, no Musashi-1 (Msi-1)-positive cells were detected (Fig. 6e), whereas on the left side, which corresponds to the region of injury and MSC transplantation, many Msi-1-positive neural stem cells were observed (Fig. 6f). Under higher magnification, Msi-1-positive cells presented red fluorescence localized to the cytoplasm, with nuclei stained with Hoechst (arrows, Fig. 6f). A coronal section of the monkey brain was analyzed for Pax-6 expression, in which the left (L) and right (R) hemispheres are delineated by a central dashed line (Fig. 6g). Consistent with the pattern observed, while immunofluorescence staining revealed no paired box 6 (Pax6)-positive neural stem cells in the right hemisphere of the monkey brain (Fig. 6h), a substantial population of such cells was detected in the left hemisphere (Fig. 6i). Upon microscopic examination at higher magnification, Pax6-positive cells displayed red fluorescence that was localized to the nucleus and colocalized with Hoechst nuclear dye (arrows, Fig. 6i). Subsequent quantitative analysis of Nestin-, Msi-1-, and Pax6-positive neural stem cells across the left and right hemispheres revealed that the relative fluorescence density of these markers was significantly greater in the left hemisphere than in the right hemisphere ($p < 0.001$, Fig. 6j). Our analysis of

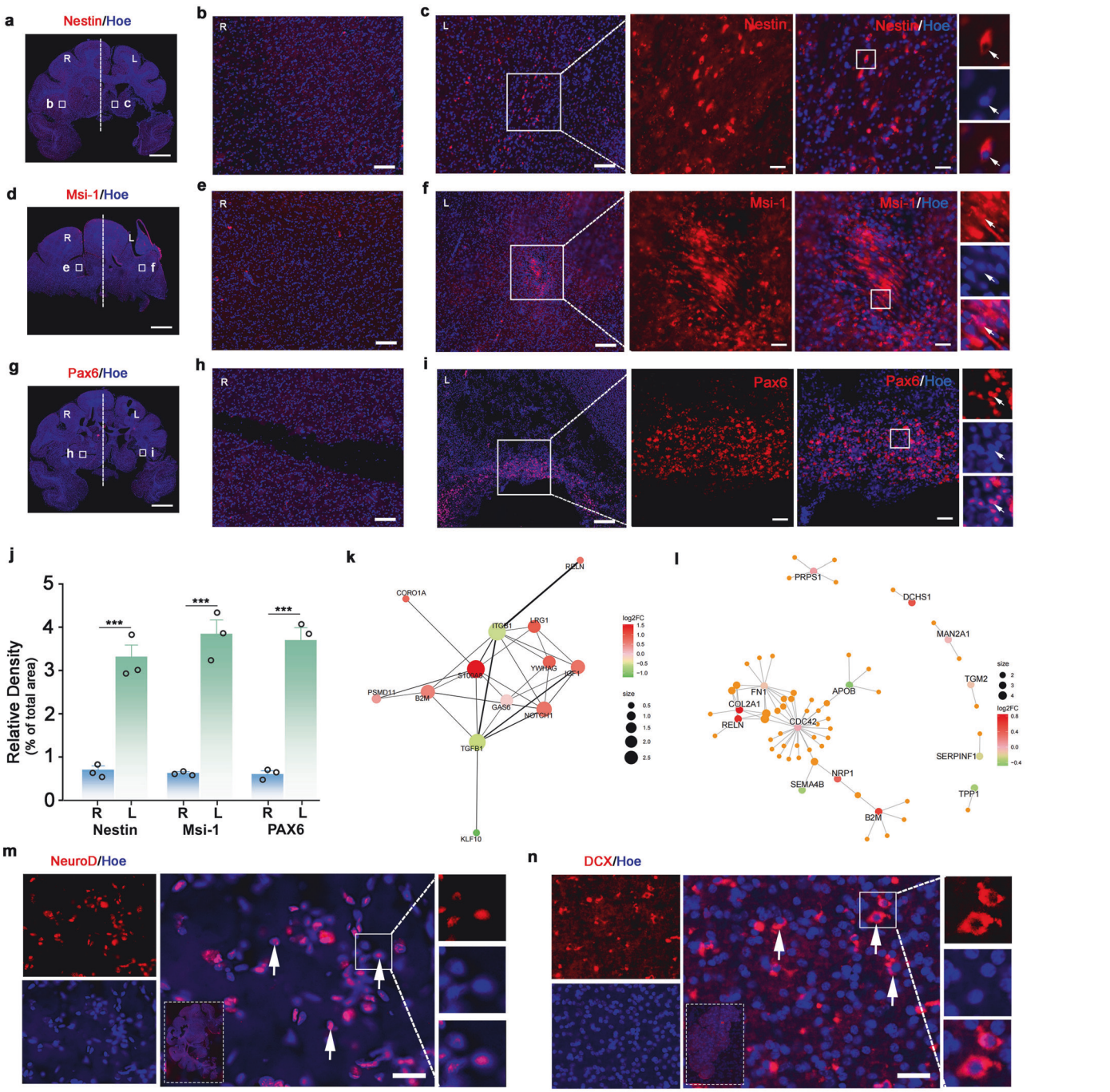

Fig. 6 Immunohistochemical staining of monkey brain tissue and plasma differential protein enrichment and interaction analysis. The ROIs shown in (**a**, **d**, **g**) were strategically defined in the parenchyma surrounding the MSC transplantation sites and the chronic infarct area. **a** Panoramic coronal section of a monkey brain immunostained for Nestin. **b** High-magnification view within the boxed area of the right hemisphere in (**a**). **c** High-magnification view within the boxed area of the left hemisphere in (**a**). Details of the boxed area showing Nestin-positive cells (arrows). **d** Msi-1 immunofluorescence staining of monkey brain coronal sections. **e**, **f** High-magnification views within the boxed areas of the right and left hemispheres in (**d**), respectively. Detailed view of the boxed region showing Msi-1-positive cells (arrows). **g** Pax6 immunofluorescence staining of coronal sections. **h**, **i** Enlarged view within the boxed area of the right and left hemisphere in (**g**), respectively. High-magnification image of the boxed region in (**g**), highlighting Pax6-positive cells (arrows). **j** Bar chart showing the quantification of the relative densities of Nestin, Msi-1, and Pax6 (***$p < 0.001$; $n = 3$). **k** A network diagram of proteins associated with neurogenesis was constructed via enrichment analysis. Each node is color-coded on the basis of its Log2FC value. **l** Protein–protein interaction network map associated with stem cell activation; the color represents the Log2FC value. **m** High-power immunofluorescence staining of NeuroD-positive cells in brain tissue (arrows). Inset: Low-magnification image with the red rectangle denoting the high-power imaging region. Higher-magnification view of the boxed area in (**m**) showing the nuclear localization of NeuroD. **n** DCX-positive cells at high magnification (arrows). Inset: Low-magnification image with the red box indicating the imaged region. Higher-magnification view of the boxed area in (**n**), confirming cytoplasmic DCX localization. Scale bars = 5 mm in (**a**, **d**, **g**); 200 μm in (**b**, **c**, **e**, **f**, **h**, **i**); 40 μm in the right panels of (**c**, **f**, **i**, **m**, **n**)

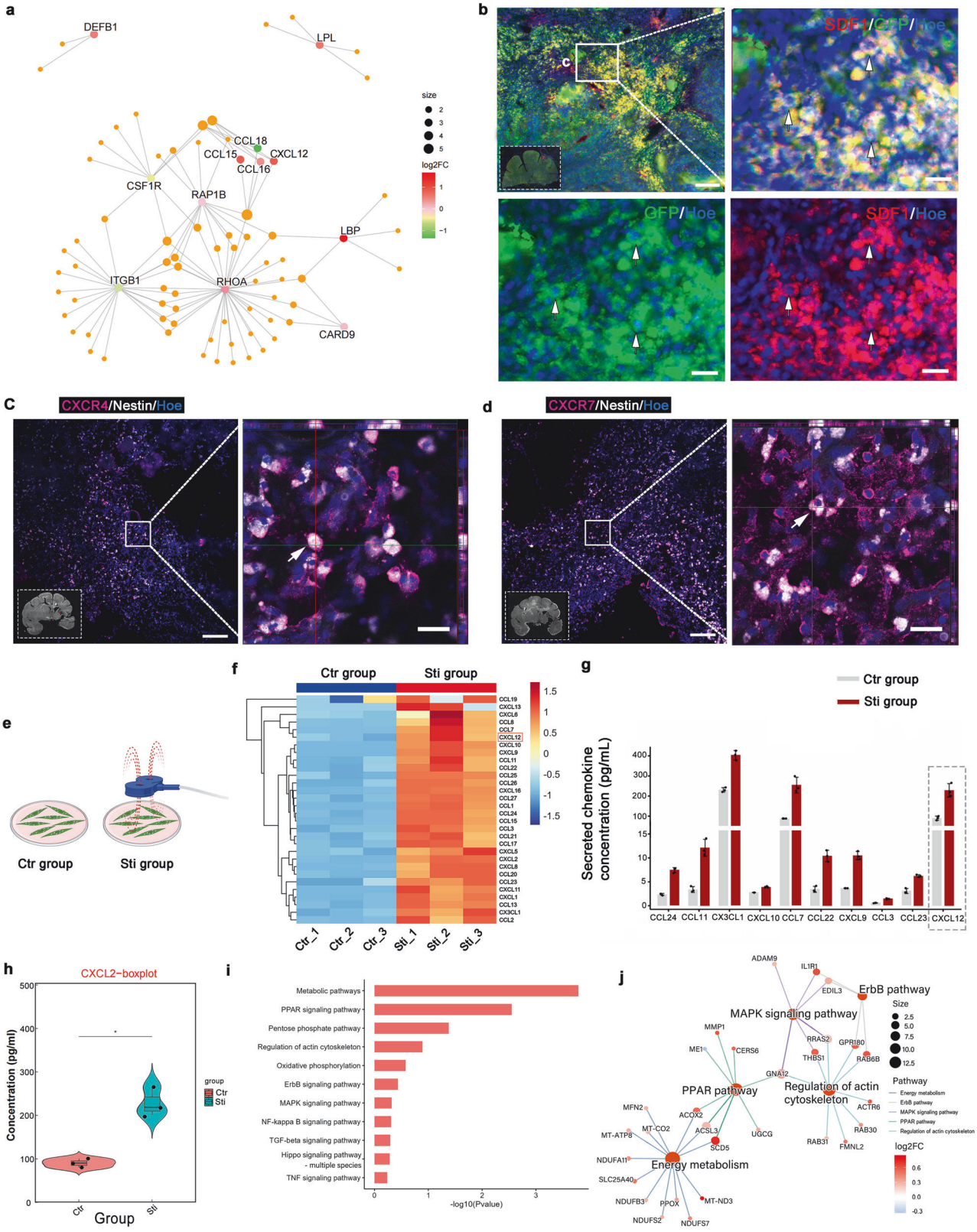

differentially expressed proteins associated with neural stem cell activation further supported the above results. The analysis revealed substantial upregulation of numerous proteins linked to stem cell activation, suggesting an enhanced role in this biological process. Moreover, these proteins exhibited a notable degree of interaction (Fig. 6k). Enrichment analysis facilitated the construction of a protein interaction network map associated with neurogenesis functions. The findings revealed that the majority of neurogenesis-related proteins were upregulated, indicating increased activity in this biological process. Furthermore, these

Fig. 7 Immunohistochemical staining of SDF1 and its receptors, Luminex liquid suspension chip detection and proteomic analysis. **a** Network diagram of chemotactic-associated proteins. Nodes are color-coded on the basis of their log2-fold change (log2FC) values. **b** SDF1 (CXCL12) immunofluorescence staining in monkey brain tissue showing SDF1-positive cells within the brain tissue (arrows). The inset box in the lower left corner is a low-magnification panoramic view. **c** CXCR4 (a recipient of CXCL12) and Nestin immunofluorescence staining of monkey brain tissue. The inset box in the lower left corner is a low-magnification panoramic view. High-magnification laser confocal orthogonal image of the boxed region showing the colocalization of CXCR4 and Nestin (arrow). **d** CXCR7 (another recipient of CXCL12) and Nestin immunofluorescence staining of monkey brain tissue. The inset box in the lower left corner is a low-magnification panoramic view. High-magnification laser confocal orthogonal image of the boxed region showing the colocalization of CXCR7 and Nestin (arrow). **e** Schematic diagram of the magnetic stimulation of MSCs in vitro. **f** Chemokine protein levels in the supernatant of MSCs from the Ctrl (control) and Sti (stimulation) groups were measured via a Luminex liquid suspension chip, and the color represents the Log2FC value. **g** Bar chart showing the concentrations of the top ten chemokines with the greatest expression level differences between the two groups. **h** Violin plot showing the CXCL12 concentration in the two groups (*$p < 0.05$; $n = 3$). **i** KEGG pathway enrichment analysis of the differentially expressed proteins in the MSCs of the two groups. **j** The protein–protein interaction network diagram showing the functional set and signaling pathways enriched with the differentially expressed proteins. The node size represents the number of candidate proteins, and the color gradient indicates the log2-fold change (log2FC) in the expression level. Scale bars = 200 μm in the upper-left image of (**b**), the left panels of (**c**, **d**); 40 μm in the upper-right image of (**b**), and the bottom panel of (**b**); 20 μm in the right panels of (**c**, **d**)

proteins exhibited a significant degree of interaction, suggesting that a complex network of communication may be critical for the regulation of neurogenesis during this process (Fig. 6l).

We subsequently identified a significant population of cells within the transplantation region of the monkey brain that expressed early neuronal markers, including NeuroD (neurogenic differentiation 1) and DCX (doublecortin). Immunofluorescence analysis revealed that NeuroD-positive cells exhibited red fluorescence within the nucleus (indicated by the arrow in Fig. 6m), and high-magnification images revealed colocalization with the nuclear dye Hoechst (Fig. 6m). A large number of DCX-positive cells were also detected (indicated by the arrows in Fig. 6n), showing red fluorescence in the cytoplasm under high-power microscopy, and the nuclei were labeled with Hoechst (Fig. 6n). The positive staining of NeuroD and DCX, which are markers of immature neurons, further supports the neuronal differentiation progression of activated neural stem cells during neurogenesis induced by mesenchymal stem cell transplantation combined with magnetic stimulation intervention.

Immunofluorescence histochemical staining and proteomic analyses revealed that the treatment stimulated endogenous neural stem cell activation, neurogenesis, and neuronal differentiation in chronic stroke monkeys.

iTBS enhances MSC chemokine secretion

Differential protein enrichment analysis conducted before and after treatment revealed the upregulation of the expression of chemokine-associated proteins, notably CXCL12 (C-X-C motif chemokine ligand 12), also referred to as stromal cell-derived factor-1 (SDF-1), which is implicated in stem cell recruitment. Furthermore, intricate interactions have been identified among these chemotaxis-related proteins, suggesting that these chemokines may play critical roles in the migration and activation of neural stem cells (Fig. 7a). The expression of SDF-1 in the transplanted MSCs in the brain tissue was further detected by immunofluorescence staining, and the results revealed that a significant number of the transplanted MSCs expressed SDF-1 (CXCL12), which manifested as positive red fluorescence, and were colabeled with the green fluorescence carried by the transplanted cells, resulting in a yellow fluorescence signal, as indicated by the arrows (Fig. 7b). Moreover, the expression of the chemokine CXCL12 receptor was detected in neural stem cells subjected to injury/transplantation. Confocal orthogonal images of the immunofluorescence staining results revealed that Nestin-positive neural stem cells also expressed CXCR4 and CXCR7 (both of which are receptors for CXCL12, as indicated by the arrows in Fig. 7c, d).

These findings suggest that the activation and aggregation of neural stem cells at the injury/transplantation site following treatment may be attributed to the chemotactic influence of the transplanted MSCs. To further depict the possible effects of magnetic fields on MSCs, a battery of in vitro tests were carried out. First, the potential toxic side effects of iTBS magnetic stimulation on SPION-loaded MSCs were ruled out by PI dye (a fluorescent nucleic acid-binding dye used to label apoptotic and necrotic cells) (Supplementary Fig. 6a). The results revealed virtually no PI-positive cells in the iTBS, SPIN, or iTBS+SPION groups (Supplementary Fig. 6b–d). In contrast, many PI-positive cells appeared in the erastin group, a classic ferroptosis inducer used as a positive control to trigger extensive MSC death (Supplementary Fig. 6e). The differences between the erastin group and the other three groups were statistically significant (Supplementary Fig. 6f). These results indicate the safety of iTBS for SPION-loaded MSCs. Next, cytokine Luminex liquid suspension chip detection and proteomic detection of cells were conducted to explore the possible molecular mechanism of iTBS in cultured MSCs (Fig. 7e). The Luminex liquid suspension chip results revealed that magnetic stimulation significantly enhanced the secretion of chemokines by MSCs. A heatmap analysis revealed that the levels of numerous chemokines were elevated in the stimulated (Sti) group compared with the nonstimulated control (Ctr) group (Fig. 7f). Quantitative analysis via a bar chart (Fig. 7g) revealed the upregulation of ten key chemokines, including CXCL12, a key mediator of stem cell recruitment, in the stimulated group. This factor alone resulted in a marked 2.5-fold increase in secretion following stimulation ($p < 0.05$, Fig. 7h). The mechanism by which magnetic stimulation increases the ability of MSCs to secrete chemokines is unclear. We subsequently conducted proteomic analysis on the MSCs in the two groups and KEGG pathway enrichment analysis of the differentially expressed proteins. The results indicated that magnetic stimulation triggered the energy metabolism pathway, the PPAR signaling pathway, the MAPK pathway, the ErbB pathway, etc. (Fig. 7i). The protein–protein interaction networks of the proteins related to these pathways were analyzed, and the results revealed that the differentially expressed proteins were related mainly to energy metabolism, cytoskeleton regulation, the PPAR pathway, the MAPK pathway, and ErbB pathway signal transduction. These proteins exhibited significant interactions with each other, indicating that complex biological network interactions are involved in the regulation of MSCs by magnetic stimulation (Fig. 7j).

These results indicate that magnetic fields increase the expression and secretion of CXCL12, a potential cytokine that can activate the chemotaxis of NSCs expressing CXCR4 and CXCR7, from MSCs.

DISCUSSIONS

The aim of this study was to investigate the therapeutic effects and mechanisms of human umbilical cord-derived MSC transplantation combined with iTBS intervention in nonhuman

primates with chronic-stage ischemic stroke. Ischemic stroke is characterized by irreversible damage to nerve tissue following the death of brain cells in the affected area due to a disruption or reduction in the blood supply to the brain. Further neurological recovery is often limited in the chronic stage of stroke once a plateau is reached. However, even marginal improvements in functional outcomes can profoundly influence the quality of life of patients with chronic stroke; therefore, new treatments are warranted. In this study, the results revealed that following the combined intervention of MSC transplantation and iTBS, the monkeys exhibited notable behavioral improvements compared with their pretreatment state. Specifically, there was a significant reduction in the resting motor threshold and latency of cortical evoked potentials. Concurrently, the intensity of brain activity, the consistency of neuronal activity, and brain functional connectivity were markedly enhanced, indicating positive therapeutic outcomes. Further exploration of the underlying mechanism revealed that this combined treatment modality further facilitated chemokine secretion, playing a pivotal role in activating and recruiting endogenous neural stem cells to the injury site. These results suggest that the synergistic interaction between MSC transplantation and iTBS stimulation could trigger a cascade of beneficial events, thereby promoting neural repair and functional recovery. The findings from the present study, which involve a clinically relevant chronic stroke NHP model, may offer some value for future clinical translation.

Mesenchymal stem cells, with their unique multidirectional differentiation potential, immune regulation, and paracrine functions, offer a new avenue for nerve regeneration and repair.[30] The long-term survival of MSCs in vivo after transplantation is challenging to achieve. Many preclinical studies have utilized various tracking methods to observe only the short-term survival of transplanted cells, which typically lasts less than two weeks.[31] In this study, the long-term survival of MSCs (over four months) was successfully achieved, as confirmed by tracking transplanted stem cells via SPION labeling technology in vivo. This tracking technology has been employed in several studies to track transplanted stem cells and has yielded promising results.[32,33] During the experiment, we utilized MRI to visualize the density shadows of stem cells labeled with SPIONs, which enabled us to track their locations and monitor changes over time in vivo. At the 17th week post-transplantation, the density of the stem cells had decreased. Accordingly, we concluded the experiment at this specific time point, which offered significant guidance for establishing the experimental endpoint. After the animals were perfused for sampling, we obtained morphological evidence of the survival of the transplanted stem cells at more than four months post-transplantation via Prussian blue staining and fluorescence observation. We tracked the survival of transplanted mesenchymal stem cells through the aforementioned multimodal tracing methods, which provide critical analytical means for comprehensively analyzing the relationship between donor survival and neurological functional improvement while offering crucial morphological evidence for in-depth investigations of the key mechanisms by which mesenchymal stem cells repair chronic stroke brain tissue. Indeed, the unequivocal survival of donor cells provides analyzable histological specimens essential for understanding their distribution within the brain parenchyma and their interactions with brain tissue components, particularly neural stem cells closely associated with regeneration. Notably, MRI revealed that the transplanted MSCs largely remained at the injection site, with no evidence of extensive migration. The observation of limited donor MSC migration is consistent with other studies of local intraparenchymal MSC transplantation.[34,35] Therefore, the therapeutic function of MSCs is likely mediated mainly by the role of MSCs residing in the damaged niche.

The sequence and timing of therapeutic interventions are critical for neural plasticity and functional recovery. The sequential application of MSC transplantation followed by iTBS aligns with the 'three-step model' proposed by Wahl and Schwab for poststroke treatment regimens,[36,37] which highlights that growth-promoting interventions should precede activity-dependent training rather than be applied simultaneously to avoid aberrant axonal branching and poor outcomes. In line with this principle, in this study, iTBS was applied one week after MSC delivery to allow sufficient time for the donor cells to establish a pro-regenerative microenvironment before subsequent iTBS-initiated neuromodulation. The sequential application of these treatments may help stabilize functional connections to avoid maladaptive rewiring. Notably, the findings from this study suggest that properly timed MSC and iTBS interventions can effectively reopen the therapeutic window for neural plasticity even at the chronic stage of central nervous system injury.

The MEP test revealed that the treatment decreased the resting motor threshold (RMT) and shortened the latency time in all monkeys. A lower RMT means that the cortex is more excitable, which is a good sign of neural function recovery.[38] Notably, two monkeys (11692 and 11685) did not show MEPs before treatment, even when 100% MSO was applied. However, their MEPs were detectable from the 5th week after treatment until the end of the study. Indeed, MEPs are tightly linked to motor recovery in the clinic. Patients without evoked MEPs often have less favorable motor outcomes than those with MEPs.[39,40] Additionally, the shortened latency of MEPs after treatment represented accelerated nerve conduction[41] and likely improved neural function outcomes.[39] This result may imply regeneration and repair of nerve fibers, leading to rebuilding of the interrupted motor pathways. Indeed, fMRI confirmed that the intensity of neural activity, neural synchronization, and active functional connectivity in the sensorimotor cortex were significantly enhanced after treatment. Additionally, DTI revealed increased directional consistency of white matter tracts. Studies have shown that iTBS can increase the number of newly formed oligodendrocytes,[42] increase the length of internodes, and increase myelination,[43] which in turn increases the speed of action potential conduction. On the other hand, although the RMT and latency eventually decreased at the end of this study, their values fluctuated at different time points after treatment. This may be due to neuroplasticity or readjustment of neural function during circuit repair.[44,45] Similarly, neural activity, synchronization, and functional connectivity, as evaluated by fMRI, also fluctuated at different time points after treatment but improved gradually and steadily until the end of the study. The process of self-repair and changes in neuroplasticity in the brain is inherently dynamic.[46] Additionally, rebalancing neural circuits within local circuits or between cerebral hemispheres as interrupted following stroke is a lengthy and gradual process.[47,48]

MRS revealed bilateral sensorimotor cortex upregulation of tNAA (neuronal integrity marker,[49]) tCho (membrane stability/acetylcholine precursor,[50]) Tau (microtubule stabilization enhancing synaptogenesis,[51]) and PCh (phospholipid metabolism intermediate.[52]) Posttreatment PCh elevation indicates enhanced membrane repair, which contrasts with stroke-induced decreases in phospholipid metabolism impairment.[53] A decrease in the level of Lac (a glycolytic end-product that accumulates in hypoxia[54]) suggested improved tissue oxygenation, potentially mediated by MSC-induced angiogenesis[55] and cytokine effects.[56] Concurrent Asp/GABA elevation reflects bidirectional neuromodulation, whereas Gln upregulation implies astrocyte-supported Glu/Gln cycle enhancement via MSC metabolic support.[57]

Plasma proteomics and, in particular, brain spatial proteomics analysis revealed that the therapeutic mechanism of the MSC-iTBS strategy involves not only cytokines, anti-inflammatory and immune regulation, neural activation and synaptic formation but also neurogenesis and chemotactic recruitment mechanisms. Enrichment analysis of chemotaxis-related proteins revealed that

many proteins were upregulated and interacted with each other. Among these, CXCL12 (also known as stromal cell-derived factor-1, SDF-1) stands out as a key chemokine involved in the chemotaxis of neural stem cells (NSCs).[58] A study involving intravenous autologous MSC transplantation in patients with severe middle cerebral artery infarction reported increased serum CXCL12 levels posttransplantation, with clinical improvement associated with elevated SDF-1 levels.[22] CXCL12 is a cytokine involved in the secretion profile of MSCs.[59] Our assays revealed CXCL12 expression in transplanted MSCs and concurrent expression of its receptors CXCR4/CXCR7 in activated endogenous NSCs, indicating a potential role for MSC-derived CXCL12 in mediating NSC migration. The Luminex liquid suspension chip also validated the significant upregulation of CXCL12 in cultured MSCs following magnetic stimulation. In addition, studies have shown that mesenchymal stem cells (MSCs) positively influence neural stem cells (NSCs), increasing their proliferation rate and activating their biological behaviors through the Notch-1 signaling pathway.[60] These findings suggest that the transplanted MSCs in this study may activate endogenous NSCs in stroke animals. Further examination of NSCs in monkey brain tissue revealed a significant number of Nestin-, Msi-1-, and PAX6-positive NSCs at the transplant/injury site, with numbers significantly differing from those on the contralateral side. Accordingly, many differentially expressed proteins related to neurogenesis and stem cell activation were enriched and closely related to two functional modules. Research has indicated that iTBS can promote the differentiation of human induced pluripotent stem cells into neurons.[61] Indeed, a significant number of naive neurons positive for Neuro D and DCX were detected in monkey brain tissue, possibly because the transplanted MSCs promoted the proliferation of many endogenous neural stem cells, whereas iTBS promoted their differentiation into neurons. Although the upregulation of early-stage markers indicates successful activation of the neurogenic niche, definitively establishing the functional integration and causal role of new neurons would require further investigation in future studies. Therefore, through both cell culture models and brain tissue section analyses, we demonstrated that magnetic stimulation effectively enhances CXCL12 production in transplanted MSCs. This phenomenon may constitute a key factor enabling donor cells to chemically induce the migration of NSCs from subventricular and local stem cell pools.

The robust endogenous neurogenesis observed in this study is likely attributed to the strategic multisite transplantation of MSCs, which effectively engaged neural stem cells (NSCs) from multiple origins. While the subventricular zone (SVZ) represents a canonical neurogenic niche for cortical repair after stroke,[62,63] accumulating evidence underscores the critical role of locally derived injury/ischemia-induced stem/progenitor cells (iSCs/iNSPCs) residing within the parenchyma.[64,65] Recent studies have indicated that in mouse models of ischemic stroke, MSCs transplanted into the peri-ischemic areas preferentially activate local residing iSCs/iNSPCs rather than distant SVZ-derived NSCs.[66] These findings demonstrate that the types of activated endogenous stem/progenitor cells are niche dependent and differ according to the MSC transplantation site. Accordingly, our experimental design, in which MSCs are administered at the SVZ margin, the ischemic penumbra, and the intermediate point, was explicitly designed to establish a comprehensive "recruitment field" capable of harnessing NSCs from both sources. We hypothesized that transplanted MSCs located near the SVZ predominantly facilitate the activation of SVZ-derived NSCs.[63] Concurrently, transplanted MSCs within the peri-infarct penumbra are inferred to primarily activate local iSCs/iNSPCs. NSCs from both sources may subsequently contribute to repopulating damaged tissue following CXCL12-guided ectopic migration, a mechanism supported by the finding that iTBS-stimulated MSCs significantly upregulate CXCL12 secretion. The functional improvement observed in all the subjects suggested that the synergistic MSC/iTBS intervention created a proregenerative microenvironment across the lesioned hemisphere. Within this milieu, the summed output of NSCs from different origins underpinned sustained neurological recovery, highlighting the therapeutic advantage of multiple-point MSC microinjection.

Importantly, repeated surgical procedures and anesthetic exposures may act as potential confounders of functional recovery following the combination treatment of MSC transplantation and iTBS. Studies have shown that surgical procedures and anesthesia can induce neuroinflammation, impair neurogenesis and hinder neurological recovery.[67–69] Therefore, despite the observation of definitive, progressive, and sustained functional improvement, the real therapeutic efficacy of the combined treatment may have been compromised by these potential confounders, particularly repeated anesthesia. On the other hand, patients are free of the burden of additional anesthesia. Therefore, combination treatment is likely to present a safe profile and greater benefit in the clinic.

This study has several limitations that should be addressed. First, despite alignment with the exploratory scope and ethical imperatives of NHP research,[70,71] the sample size is small. Future studies with larger cohorts are therefore necessary to confirm the robustness, effect size, and reproducibility of combined MSC/iTBS therapy. Second, this study employed a within-subjects (self-controlled) design. Consequently, it cannot be differentiated whether the observed recovery stems from a synergistic interaction or merely additive effects of the combined therapy. Future studies utilizing a full factorial design are needed to delineate the specific contributions and synergies of each component. Third, key challenges for clinical translation include the inherent invasiveness of the injection protocol and the lack of long-term safety assessment within 17-week study. Although the absence of acute adverse events (e.g., seizures, significant inflammation) is an encouraging preliminary finding, successful translation may ultimately depend on developing minimally invasive delivery techniques and obtaining data from extended safety studies. Despite these limitations, the internal consistency of the data across complementary measures and the profound translational relevance of the NHP model provide a strong rationale for the observed therapeutic effects. These promising results warrant further investigation in expanded preclinical cohorts as a critical step toward potential clinical translation.

In conclusion, in an NHP model, the combined application of MSC transplantation and iTBS intervention promoted multimodal recovery from chronic stroke. This combination treatment regimen achieved long-term MSC survival in the injured-side brain parenchyma and led to measurable improvements in motor function. It concurrently elevated cerebral cortical excitation thresholds, reduced MEP latency, augmented neural activity intensity and synchronization patterns, reinforced positive functional brain connectivity, and improved metabolic activity within the motor cortex. The underlying mechanisms may be mediated by cytokine-mediated signaling, anti-inflammatory and immunomodulatory effects, neural circuit activation through synaptic plasticity enhancement, chemotactic recruitment of endogenous neural stem cells, and their subsequent proliferation and differentiation. Magnetic stimulation effectively enhances the production of CXCL12 from MSCs, which could be a pivotal factor by which donor cells chemically induce the migration of endogenous NSCs in the subventricular stem cell pool and local NSCs. This investigation developed an innovative interdisciplinary therapeutic strategy for chronic stroke management that integrates MSC-based cellular therapy with iTBS transcranial magnetic neuromodulation. Through multilevel analysis of therapeutic outcomes and potential mechanisms, this work establishes both a novel treatment paradigm and a translational framework for clinical applications in chronic stroke rehabilitation.

MATERIALS AND METHODS

Ethics approval

All animal-related research activities in this study were approved by the Animal Care and Use Committee of the Guangdong Laboratory Animal Monitoring Institute (Approval No. IACUC2020158).

Experimental animals

Three male *Macaca fascicularis* macaques (10–12 years, 6.8–9.5 kg; IDs: 11685/11688/11692) sourced from the Huazhen Animal Breeding Farm (Conghua) were subjected to left MCAO modeling via electrocoagulation. After the procedure, the monkeys were individually housed at Guangdong Animal Monitoring Institute under controlled conditions: 19–23 °C, 40–70% humidity, a 12 h light/dark cycle (08:00–20:00 light phase), and two daily commercial pellet feedings (~09:00/16:00) supplemented with fresh produce provided in the afternoon.

Experimental procedure

Initially, the MCAO stroke model was established in *Macaca fascicularis*. Regular postoperative care and rehabilitation procedures were applied. In the chronic phase of stroke (24 months after stroke), GMP-grade, biolabeled human umbilical cord-derived MSCs were stereotaxically injected into the penumbra area of the brain following MRI-based diagnosis. Starting three days before the transplantation surgery, daily subcutaneous injections of cyclosporine were applied to reduce immune rejection to the donor cells. Transcranial iTBS commenced 1 week post-transplantation at 5 sessions per week until the experimental endpoint (17 weeks post-transplantation). Behavioral studies were evaluated at the following time points: the 6th month, 5th month, and 1st week before the start of treatment (serving as baseline) and at the 5th, 9th, 13th, and 17th weeks after treatment. MRI analysis was performed 1 week before treatment (baseline) and at the 1st, 5th, 9th, 13th, and 17th weeks after treatment. Electrophysiological analysis was performed 1 week before treatment (baseline) and at the 5th, 9th, 13th, and 17th weeks after treatment. MRS, fMRI, and DTI were performed at the 1st week before treatment (baseline) and at the 1st, 5th, 9th and 17th weeks after treatment. Plasma samples were collected at the 1st week before treatment (baseline) and at the 17th week after treatment. Brain tissue samples were obtained at the end of the study (i.e., the 17th week after treatment).

MCAO stroke model

Preoperative preparations for *Macaca fascicularis* macaques included 12 h of fasting and aseptic site preparation (shaving/povidone-iodine disinfection). Anesthesia was maintained with 1.5–3% isoflurane in 100% O_2, with continuous monitoring of vital signs (heart rate, blood pressure, respiratory rate, and temperature). Mechanical ventilation stabilized respiratory parameters with adjunctive intravenous saline/5% glucose, maintaining fluid–electrolyte balance. A left pterional approach was initiated with monopolar electrocautery for scalp incision, followed by scalpel dissection through the muscular layers to expose the skull. Under microscopic guidance, a craniotomy was performed via a high-speed drill with bone flap removal. The left middle cerebral artery was isolated at the lateral sulcus with microscissors, occluded by bipolar electrocautery, and transected to ensure complete occlusion. Layered closure of the muscle and skin was used to perform the procedure. Subsequently, 20 ml of a 20% mannitol solution was administered intravenously to mitigate the risk of cerebral edema. After the procedure, the monkeys received postoperative care for two weeks, which included the administration of ampicillin (0.1 g/kg, intramuscular injection, twice daily) to prevent infection, tramadol (0.5 ml/day, intramuscular injection) to alleviate pain, mannitol (0.2–2 g/kg, intravenous injection) to reduce cerebral edema, and parenteral nutrition.

Culture and labeling of human MSCs

In this study, we utilized clinical-grade human umbilical cord MSCs that adhered to good manufacturing practice (GMP) standards provided by the National Institute of Stem Cell Clinical Research, Guangdong Provincial Hospital of Chinese Medicine, a facility conducting stem cell clinical trials accredited by the National Health Commission of China. Human umbilical cord-derived MSCs at passages 7–9 were used in this study, and the preparation method was consistent with that used in a previous study.[34] Briefly, the cells were digested in 0.25% trypsin/0.02% EDTA, centrifuged (1000 rpm, 5 min), and subcultured at 1:8 upon reaching 80% confluence. The donor MSCs were prelabeled with FITC-conjugated SPIONs before transplantation,[33] and 10 nM (20 μg/mL) FITC-conjugated SPIONs (SunLipo NanoTech, China) were added to the cell suspension and incubated for 30 minutes. After centrifugation, the cells were washed with Hank's solution three times and then subjected to the next step for testing or transplantation. This labeling technology combines the advantages of magnetic and fluorescent labeling. Superparamagnetic iron nanoparticles have low signals in MR-T2 images, allowing noninvasive and accurate tracking and monitoring of stem cells in living individuals after transplantation. In addition, during morphological analysis, the transplanted cells could be visualized by FITC-emitting green fluorescence or Prussian blue staining to probe the iron nanoparticles.

Transmission electron microscopy

Transmission electron microscopy (TEM) was performed on two-dimensional cultured MSCs to observe the presence of SPIONs within the cells. MSCs were cultured on glass slides. After the culture medium was removed, the cells were fixed with a solution of 4% paraformaldehyde (PFA) and 3.5% glutaraldehyde for 30 minutes. The subsequent steps included gradient ethanol dehydration, acetone replacement, and Epon infiltration. The resin block was then inverted on the slide for polymerization at 60 °C for 48 h. After the slide was peeled off, the sample was cut into ultrathin sections via an ultramicrotome. These sections were mounted on copper grids and stained with lead uranyl acetate. The samples were then observed and photographed via a transmission electron microscope (FEI TECNAI-G2 SPIRIT).

MSC transplantation surgery

Preterm MCAO monkeys were fasted for 12 hours and then anesthetized via intramuscular injection of a ketamine-xylazine-atropine cocktail (10 mg/kg, 2 mg/kg, or 0.05 mg/kg). Following midline craniotomy, stereotaxically guided injections were administered at nine coordinates determined by the *Macaca fascicularis* brain atlas and T2-MRI. The sites targeted the SVZ margins, ischemic penumbra, and intermediate points between them and were supplemented rostrocaudally (±2 mm) to form a 3 × 3 grid. At each site, 8 μl of stem cell suspension (1.6×10^5 cells) was injected via a Hamilton microliter syringe, with needles retained in situ for 3 min post-injection. Anesthesia was maintained with 1.5–3% isoflurane/100% O_2, supplemented by intravenous 20% mannitol (20 ml) for intracranial pressure control. Vital signs were continuously monitored during surgery. Postinjection, the puncture sites were sealed with bone wax, followed by layered closure of the muscle/skin. Postoperative care included thermoregulation until consciousness recovery and twice-daily ampicillin sodium (0.1 g/kg) for 5 days.

Transcranial magnetic stimulation

A two-week period of behavioral training and acclimation to the TMS facility was implemented before starting the experiment. To apply TMS, awake monkeys were fastened to a special seat, and iTBS (intermittent theta-burst stimulation) was administered to the hotspot on the injured side via a figure-eight coil (1.96 T, YRD CCY1, Wuhan Yiruide Medical Equipment, China). iTBS employs a

sequence of stimuli characterized by bursts of three pulses, each administered at a frequency of 50 Hz. These bursts are delivered repetitively at a frequency of 5 Hz, with each burst occurring every 200 milliseconds, creating a high-frequency stimulation pattern. Each cycle of iTBS lasted for 2 s, followed by an 8-second interval. The entire protocol encompasses a total of 600 pulses distributed across 20 cycles, with the complete treatment lasting approximately 200 s. The stimulation intensity was adjusted to fall within the range of 70% of the resting motor threshold (RMT).

Behavioral evaluation

The behavioral evaluation of stroke monkeys includes three items: the hill-staircase task (Supplementary video 1), the valley-staircase task (Supplementary video 2), and the object retrieval task (Supplementary video 3). Behavioral equipment developed by the team of the Guangdong Laboratory Animal Monitoring Institute was used to evaluate the unilateral motor ability of the animals. The equipment consists of two parts, the hill staircase and the valley staircase, and the design is based on the work of Marshall and Mcentire.[72,73] The experiment was conducted three times daily for 5 days to obtain the average score. The object retrieval task apparatus, engineered by the Guangdong Provincial Laboratory Animal Monitoring Institute, refers to the design of Mcentire and colleagues[73] and consists of a test cage, an adjustable transparent resin barrier, a transparent square container with a one-way opening, and a transparent workbench. The task was used to record the mean time for successful retrieval with the right hand and measure the frequency of right-hand use. The detailed experimental procedures for the three tasks are provided in the Supplementary Materials.

Electrophysiological detection

Electrophysiological assessments were conducted with a CCY-IA magnetic field stimulator (Yiruide). Following anesthesia administration, surface electrodes were then applied to the belly and tendon of the first dorsal interosseous muscle with conductive gel, while a ground electrode was placed on the contralateral upper limb. Upon initiation of the EMG recording device, the stimulation sequence began with single-pulse stimulation, incrementally mapping the cortical regions that elicit significant motor-evoked potentials (MEPs) starting at 60% of the maximum stimulator output (MSO). Once an effective stimulus site was identified, it was marked (i.e., the hotspot), and the stimulus intensity was gradually titrated down to ascertain the resting motor threshold (RMT). If no MEP was detectable at 60% MSO, the attempt was made at 100% MSO; if the MEP could still not be elicited, it was recorded as an MEP absence (MEP negative). To facilitate subsequent statistical analyses, MEP-negative data were set, at the time of analysis, to an RMT value of 100% MSO. In this study, considering the reduction in cortical excitability due to anesthetic agents, the RMT criterion was defined as the minimum stimulus intensity that must produce at least three MEPs in a series of five consecutive stimuli, with each MEP having an amplitude of at least 50 μV. The RMT and latency (LA) were meticulously recorded and analyzed.

Brain imaging

The neuroimaging data were collected via a 3.0 T magnetic resonance imaging (MRI) scanner (United Imaging, China) at the Guangdong Provincial Laboratory Animal Monitoring Institute. Prior to the imaging procedure, the monkeys were subjected to a 12 h fast. Anesthesia was administered via intramuscular injection of a ketamine-xylazine-atropine cocktail. Upon achieving deep anesthesia, the monkeys were secured in an eight-channel monkey head coil, integrated with a stereotactic apparatus, and positioned prone on the scanning platform to initiate the MRI scan. This study utilized the brain atlas delineated by Ballanger et al., encompassing 79 distinct brain regions (listed in Supplementary Table 1), with an emphasis on the analysis of 70 gray matter regions. In the context of resting-state functional magnetic resonance imaging (rs-fMRI), the primary variables of interest were the amplitude of low-frequency fluctuations (ALFF), regional homogeneity (ReHo), and functional connectivity (FC). For diffusion tensor imaging (DTI), the principal analytical focus is on fractional anisotropy (FA). The detailed data collection and processing procedures of brain imaging for the monkeys are provided in the Supplementary Materials.

Magnetic resonance spectroscopy

Magnetic resonance spectroscopy (MRS) employs magnetic resonance phenomena and chemical shift effects to conduct a quantitative analysis of metabolites within biological tissues. Using the open-source R-based toolbox spant (version 2.18.0, available at https://martin3141.github.io/spant/index.html), we performed coil combination, phase alignment, and repeat averaging. The preliminary processing steps involved coil combination, phase alignment, and repeated averaging to refine the data. The key methodological steps included spectral alignment, referencing the spectra to the total N-acetylaspartate (tNAA) peak at 2.01 ppm, and water signal removal via the Hankel singular value decomposition (HSVD) filter to mitigate residual water signals. Adaptive baseline correction was implemented through the application of the adaptive baseline fitting algorithm (ABF), facilitating fully automated routine MRS analysis. The absolute metabolite concentrations of total N-acetylaspartate (tNAA), total choline (tCho), total tau (Tau), and total phosphorylcholine (PCh) within the bilateral sensorimotor cortex (SMC) were quantified. Additionally, the absolute levels of aspartate (Asp), glutamate and glutamine combined (Glx), gamma-aminobutyric acid (GABA), myo-inositol (Ins), lactate (Lac), glutamine (Gln), glucose (Glc), and glycerophosphocholine (GPC) at the injection site area were analyzed.

Plasma collection and proteomics

After anesthesia, ~8 mL of blood/monkey was collected via femoral venipuncture under sterile conditions. The blood was transferred to EDTA tubes and centrifuged at 3000 RPM (4 °C, 20 min). The plasma was aspirated to avoid the buffy layer, aliquoted into sterile tubes, and stored at −80 °C for proteomic analysis. Aseptic techniques were maintained throughout. 4D-DIA quantitative proteomics analysis of posttreatment vs. baseline plasma protein profiles. The samples were subjected to high-abundance protein depletion via a Bio-Rad ProteoMiner™: 100 μL of plasma was incubated with the microspheres (2 h), centrifuged, and the pellet was washed with PBS, treated with 1% TFA, lyophilized, and resuspended in urea (-80 °C storage). Peptides were separated via an EASY nLC 1200 UHPLC coupled to a Q Exactive HF-X Orbitrap (nanospray source) operating in top-40 DDA mode (Orbitrap MS: 120 K resolution, 350–1500 m/z). Spectronaut v15.7 processed MS/MS data against the *Macaca fascicularis* UP000233100 proteome (50,205 sequences). For the differentially expressed proteins, $|FC| > 1.2$ and $p < 0.05$ were used.

Brain tissue harvesting and immunofluorescence staining

At the endpoint (17 weeks post-transplantation), monkeys under deep anesthesia underwent transcardial perfusion with 2000 mL of saline for blood clearance followed by 4% paraformaldehyde (PFA) infusion (30 min of fixation). The brains were extracted, postfixed in 4% PFA, and stored at 4 °C for histological analysis. Following graded sucrose dehydration (20%-30% until tissue sinking), coronal sections were dissected via a monkey brain matrix guided by imaging-identified stem cell injection/infarction areas, embedded in OCT compound (Tissue-Tek, Japan) and cryosectioned at 35 μm thickness. The sections were rinsed with 0.01 M PBS and blocked with 10% goat serum at 37 °C for 1 h. The sections were incubated with primary antibodies at 4 °C overnight,

equilibrated at RT for 30 min, and then rinsed 3 × 5 min in PBS. After washing, the sections were incubated with species-fluorescent secondary antibodies at 37 °C for 1 hr. Nuclei were counterstained with Hoechst 33342 (37 °C, 15 min), removed, and rinsed 3 × 5 min in PBS. The samples were mounted with coverslips by mounting medium and imaged via a tissue slide scanner (TissueFAXS, TissueGnostics, Austria). All the antibodies/reagents used are detailed in Supplementary Table 2.

Prussian blue staining

The Prussian blue reaction, a histochemical staining technique, was employed to detect iron ions within the donor cells in the tissue samples. This method capitalizes on the interaction between iron ions and potassium ferrocyanide present in the staining solution, resulting in the formation of an insoluble blue iron-ferrocyanide complex that can be observed. Given that the transplanted MSCs were laden with SPIONs, the brain sections were subjected to Prussian blue staining via a Prussian Blue Iron Stain Kit (Solarbio, China) to visualize the engrafted cells. The steps were as follows: the sections were washed with PBS 3 times for 5 min each and then incubated with Perls' solution at 37 °C for 20 min. The reaction was stopped by rinsing with distilled water, followed by counterstaining with eosin solution at room temperature. The samples were subsequently dehydrated via a graded ethanol series, clarified with xylene, and sealed with neutral balsam. Finally, the sections were examined via a tissue slide scanner.

Spatial proteomic analysis of FFPE tissue sections

Formalin-fixed, paraffin-embedded (FFPE) tissue sections of monkey brains were prepared for spatial proteomic analysis. Sections were collected onto slides, air-dried, and subsequently processed at 65 °C for 60 min to enhance tissue adhesion. Deparaffinization and rehydration were performed by sequential immersion in the following solutions: xylene (twice for 2 min each), 100% ethanol (twice for 1 min each), 95% ethanol, 85% ethanol, 75% ethanol, 50% ethanol, and finally ddH_2O. Following rehydration, the sections were subjected to hematoxylin and eosin (H&E) staining. Briefly, the slides were incubated with hematoxylin for 7 min, bluing buffer for 2 min, and counterstained with eosin for 40 s. The residual stain was removed by rinsing with water. The H&E-stained sections were then incubated at 37 °C for 5 min and immediately visualized via a digital slide scanner (VS200, OLYMPUS) at 20× magnification. Given that macaque brain tissues were formaldehyde fixed and mounted on slides, a low-resolution spatial proteomics approach was adopted. To ensure precise and cell type-specific sampling, the contours of the regions of interest were first defined on the digital H&E images via the PALM (Zeiss) laser microdissection system. These defined regions were then used as a precise guide for subsequent manual dissection with a scalpel. The dissected tissue fragments were carefully collected into corresponding tubes for further proteomic analysis. Proteins were extracted and digested with trypsin, and the resulting peptides were analyzed via liquid chromatography–tandem mass spectrometry (LC–MS/MS) in data-independent acquisition (DIA) mode on an Orbitrap Astral mass spectrometer. The resulting mass spectrometry data were processed via the DIA-NN search engine (v.1.8) against the *Macaca fascicularis* protein database (Macaca_fascicularis_9541_PR_20241023. fasta), and subsequent bioinformatic analysis was subsequently performed to identify the differentially expressed proteins and their associated biological pathways.

Magnetic stimulation and luminex liquid suspension chip detection in vitro

To quantify the effects of iTBS on MSC chemokine secretion via a Luminex assay (Bio-Rad #171AK99MR2), 2×10^5 MSCs/well were seeded in 6-well plates. The stimulation group (Sti group, $n = 3$) received 40% MSO iTBS (3 sessions/day × 3 days), whereas the control group (Ctr group) received acoustic sham stimulation. The supernatants were centrifuged (10 min), and 50 µL aliquots were subjected to sequential antibody incubation and streptavidin-PE (SA-PE) conjugation. Chemokine concentrations were quantified via a Bio-Plex 200 (Luminex Corporation, Austin, TX, USA) with standard curve interpolation after fluorescence detection.

Proteomics in vitro

To elucidate the alterations in the protein expression profiles of MSCs induced by magnetic stimulation, MSCs from each group ($n = 3$) were harvested after iTBS as described in Section 2.16, followed by scraping to prepare samples for proteomic analysis. The workflow involved sequential steps, including protein extraction, enzymatic digestion, and peptide desalting, culminating in LC–MS analysis. Peptides were separated via an ES906 C18 column (PepMap™ Neo UHPLC; 150 µm × 15 cm, 2 µm) with gradient elution (Buffer A: 0.1% FA/water; Buffer B: 0.1% FA/84% ACN) interfaced with an Orbitrap Astral MS. ESI-ionized peptides were subjected to DIA analysis. For the differentially expressed proteins, $|FC| > 1.2$ and $p < 0.05$ were used.

Morphological quantification

ImageJ software (National Institutes of Health, Bethesda, Maryland, USA) was used to quantify the hypo-intense regions representing transplanted stem cells in the MR images. For each monkey, the section with the largest hypo-intense region was selected for analysis, and the hypo-intense region identified in the box of the same size as the region of interest (ROI) was defined. The number of pixels within each slice ROI was measured via ImageJ software and was normalized by the total number of pixels in the box. The resulting percentage was used for statistical analysis to compare the values across different time points.

To assess endogenous neural stem cells in the brain, the nestin-, musashi-1 (Msi1)-, and Paired Box 6 (Pax6)-positive areas were quantified via ImageJ software. For each monkey, three brain slices containing the injury site were selected, and five random fields were identified in both the left and right hemispheres within each slice. The immunopositive areas were converted into ROIs under 200× magnification. ImageJ software was employed to measure the pixel count within the ROIs for each slice. Next, the fluorescence density of the Nestin-, Msi1-, and Pax6-immunostained regions was calculated for each image and normalized to the total pixel count within the image. Ultimately, a statistical analysis was conducted to compare the fluorescence density values between the left and right hemispheres.

Statistical analysis

SPSS statistics software 26.0 was used for the statistical analysis of longitudinal metrics, including behavioral scores, brain imaging, and electrophysiological records, which were collected at both pretreatment and posttreatment time points. The data are presented as the means ± standard errors of the means (SEMs). For the comparison of multiple groups, generalized estimating equations (GEEs) were utilized, followed by post hoc analyses via the least significant difference (LSD) test. Paired t tests were applied to assess differences between the two groups, with statistical significance defined as $p < 0.05$. The results were graphically represented via Origin (OriginPro 2021) and GraphPad Prism 9.0 software.

DATA AVAILABILITY

All the data generated or analyzed in this study are included in this published article and supplementary files. The mass spectrometry proteomics data have been deposited in the ProteomeXchange Consortium via the PRIDE partner repository with the dataset identifier PXD071582.

ACKNOWLEDGEMENTS

Special thanks to Dr. Si-min Wen, statistician, for serving as the analytical consultant for the statistical methods. This study was financially supported by the National Natural Science Foundation of China (81974357; 82371395; 82272588), the Natural Science Foundation of Guangdong Province (2023A1515030254; 2024A1515220057; 2024A1515010814), the Guangzhou Basic and Applied Basic Research Foundation (2023A03J0626), the Hospital Funding for Developing Stem Cell Reagent and Organoind Platform (GXB202401) and the Startup Grant of Guangdong Provincial Hospital of Chinese Medicine (2022KT1032).

AUTHOR CONTRIBUTIONS

Conceptualization: Y.L., X.Z., G.Q.X. and Y.H.M.; Data curation: Y.H.M., G.B.C., M.F.W., and X.Z.; Formal analysis: Y.H.M., G.B.C., M.F.W., G.L., Y.Z., J.P.L., M.W., L.C., C.L.Z., J.B.J., K.Z., K.J.Z., Y.L., Z.L., J.L.C., T.L. and L.X.W.; Funding acquisition: Y.L., X.Z., G.Q.X. and Y.H.M.; Methodology: Y.H.M., G.B.C., M.F.W., G.L., Y.Z., M.W., C.L.Z., J.B.J., K.Z., K.J.Z. and Y.L.; Project administration: Y.L., X.Z. and G.Q.X.; Visualization: Y.H.M., G.B.C., M.F.W.; Writing–original draft: Y.H.M. and G.B.C.; Writing–review & editing: X.Z. and Y.L.; All the authors have read and approved the article.

ADDITIONAL INFORMATION

Supplementary information The online version contains supplementary material available at https://doi.org/10.1038/s41392-026-02694-5.

Competing interests: The authors declare no competing interests.

Publisher's note Springer Nature remains neutral with regard to jurisdictional claims in published maps and institutional affiliations.

REFERENCES

1. Donkor, E. S. Stroke in the 21(st) century: A snapshot of the burden, epidemiology, and quality of life. *Stroke Res Treat.* **2018**, 3238165 (2018).
2. Global, regional, and national burden of stroke and its risk factors, 1990-2021: A systematic analysis for the global burden of disease study 2021, *Lancet Neurol*. **23**, 973-1003 (2024).
3. Christensen, H. & Pezzella, F. R. Implementation of the stroke action plan for Europe 2018-2030 during coronavirus disease-2019. *Curr. Opin. Neurol.* **34**, 55–60 (2021).
4. Ding, Q. et al. Global, regional, and national burden of ischemic stroke, 1990-2019. *Neurology* **98**, e279–e290 (2022).
5. Jørgensen, H. S. et al. Outcome and time course of recovery in stroke. Part II: Time course of recovery. The Copenhagen Stroke Study. *Arch. Phys. Med Rehabil.* **76**, 406–412 (1995).
6. Winstein, C. J. et al. Guidelines for adult stroke rehabilitation and recovery: A guideline for healthcare professionals from the American Heart Association/American Stroke Association. *Stroke* **47**, e98–e169 (2016).
7. Georgiou, A. M. & Kambanaros, M. The effectiveness of transcranial magnetic stimulation (TMS) paradigms as treatment options for recovery of language deficits in chronic poststroke aphasia. *Behav. Neurol.* **2022**, 7274115 (2022).
8. Zhu, M. et al. The effect of transcranial magnetic stimulation on cognitive function in poststroke patients: A systematic review and meta-analysis. *BMC Neurol.* **24**, 234 (2024).
9. Pabst, A. et al. A systematic review and meta-analysis of the efficacy of intermittent theta burst stimulation (ITBS) on cognitive enhancement. *Neurosci. Biobehav Rev.* **135**, 104587 (2022).
10. Huang, Y. Z. et al. Theta burst stimulation of the human motor cortex. *Neuron* **45**, 201–206 (2005).
11. Talelli, P., Greenwood, R. J. & Rothwell, J. C. Exploring theta burst stimulation as an intervention to improve motor recovery in chronic stroke. *Clin. Neurophysiol.* **118**, 333–342 (2007).
12. Suppa, A. et al. Ten years of theta burst stimulation in humans: Established knowledge, unknowns and prospects. *Brain Stimul.* **9**, 323–335 (2016).
13. Chen, G. et al. Effects of repetitive transcranial magnetic stimulation on sequelae in patients with chronic stroke: A systematic review and meta-analysis of randomized controlled trials. *Front Neurosci.* **16**, 998820 (2022).
14. Stevanovic, I. et al. Theta burst stimulation influence the expression of BDNF in the spinal cord on the experimental autoimmune encephalomyelitis. *Folia Neuropathol.* **57**, 129–145 (2019).
15. Wang, L. et al. Long-term ITBS promotes neural structural and functional recovery by enhancing neurogenesis and migration via mir-551b-5p/bdnf/trkb pathway in a rat model of cerebral ischemia–reperfusion injury. *Brain Res Bull.* **184**, 46–55 (2022).
16. Luo, L. et al. Intermittent theta-burst stimulation improves motor function by inhibiting neuronal pyroptosis and regulating microglial polarization via TLR4/NFκB/$NLRP_3$ signaling pathway in cerebral ischemic mice. *J. Neuroinflammation.* **19**, 141 (2022).
17. Liu, J. L. et al. The therapeutic mechanism of transcranial itbs on nerve regeneration and functional recovery in rats with complete spinal cord transection. *Front Immunol.* **14**, 1153516 (2023).
18. Xie, G. et al. Repetitive transcranial magnetic stimulation for motor function in stroke: A systematic review and meta-analysis of randomized controlled studies. *Syst. Rev.* **14**, 47 (2025).
19. Zhang, J. J. Y. et al. Repetitive transcranial magnetic stimulation for motor recovery after stroke: A systematic review and meta-analysis of randomized controlled trials with low risk of bias. *Neuromodulation* **28**, 16–42 (2025).
20. Dabrowska, S. et al. Neuroinflammation as a target for treatment of stroke using mesenchymal stem cells and extracellular vesicles. *J. Neuroinflammation.* **16**, 178 (2019).
21. Zheng, H. et al. Mesenchymal stem cell therapy in stroke: A systematic review of literature in preclinical and clinical research. *Cell Transplant.* **27**, 1723–1730 (2018).
22. Lee, J. S. et al. A long-term follow-up study of intravenous autologous mesenchymal stem cell transplantation in patients with ischemic stroke. *Stem Cells* **28**, 1099–1106 (2010).
23. Bang, O. Y. et al. Autologous mesenchymal stem cell transplantation in stroke patients. *Ann. Neurol.* **57**, 874–882 (2005).
24. R. Berlet, R. et al. Combination of stem cells and rehabilitation therapies for ischemic stroke. *Biomolecules*. **11**, 1316 (2021).
25. Bakreen, A. et al. Additive behavioral improvement after combined cell therapy and rehabilitation despite long-term microglia presence in stroke rats. *Int. J Mol. Sci.* **22**, 1512 (2021).
26. Galleu, A. et al. Apoptosis in mesenchymal stromal cells induces in vivo recipient-mediated immunomodulation. *Sci. Transl. Med.* **9**, eaam7828 (2017).
27. Lin, X. et al. Nonhuman primate models of ischemic stroke and neurological evaluation after stroke. *J. Neurosci. Methods* **376**, 109611 (2022).
28. Long, X. & Zeng, J. Why nonhuman primates are needed in stroke preclinical research. *Stroke Vasc. Neurol.* **10**, e003504 (2025).
29. Karabanov, A. N., Raffin, E. & Siebner, H. R. The resting motor threshold-restless or resting? A repeated threshold hunting technique to track dynamic changes in resting motor threshold. *Brain Stimul.* **8**, 1191–1194 (2015).
30. Anbari, F. et al. Intravenous transplantation of bone marrow mesenchymal stem cells promotes neural regeneration after traumatic brain injury. *Neural Regen. Res.* **9**, 919–923 (2014).
31. Ruzicka, J. et al. A comparative study of three different types of stem cells for treatment of rat spinal cord injury. *Cell Transplant.* **26**, 585–603 (2017).
32. Rosenberg, J. T. et al. Tracking mesenchymal stem cells using magnetic resonance imaging. *Brain Circ.* **2**, 108–113 (2016).
33. Kim, H. Y. et al. Therapeutic efficacy-potentiated and diseased organ-targeting nanovesicles derived from mesenchymal stem cells for spinal cord injury treatment. *Nano Lett.* **18**, 4965–4975 (2018).
34. Ma, Y. H. et al. Perineurium-like sheath derived from long-term surviving mesenchymal stem cells confers nerve protection to the injured spinal cord. *Biomaterials* **160**, 37–55 (2018).
35. Sajjad, U. et al. Exploring mesenchymal stem cells homing mechanisms and improvement strategies. *Stem Cells Transl. Med.* **13**, 1161–1177 (2024).
36. Wahl, A. S. et al. Neuronal repair. Asynchronous therapy restores motor control by rewiring of the rat corticospinal tract after stroke. *Science* **344**, 1250–1255 (2014).
37. Wahl, A. S. & Schwab, M. E. Finding an optimal rehabilitation paradigm after stroke: Enhancing fiber growth and training of the brain at the right moment. *Front Hum. Neurosci.* **8**, 381 (2014).
38. Veldema, J., Nowak, D. A. & Gharabaghi, A. Resting motor threshold in the course of hand motor recovery after stroke: A systematic review. *J. Neuroeng. Rehabil.* **18**, 158 (2021).
39. Escudero, J. V. et al. Prognostic value of motor evoked potential obtained by transcranial magnetic brain stimulation in motor function recovery in patients with acute ischemic stroke. *Stroke* **29**, 1854–1859 (1998).
40. Yen, C. C. et al. Predictive value of motor-evoked potentials for motor recovery in patients with hemiparesis secondary to acute ischemic stroke. *Ann. Med.* **55**, 2225144 (2023).
41. Milardovich, D. et al. Delmep: A deep learning algorithm for automated annotation of motor evoked potential latencies. *Sci. Rep.* **13**, 8225 (2023).
42. Cullen, C. L. et al. Low-intensity transcranial magnetic stimulation promotes the survival and maturation of newborn oligodendrocytes in the adult mouse brain. *Glia* **67**, 1462–1477 (2019).
43. Cullen, C. L. et al. Periaxonal and nodal plasticities modulate action potential conduction in the adult mouse brain. *Cell Rep.* **34**, 108641 (2021).

44. Sharbafshaaer, M. et al. Harnessing brain plasticity: The therapeutic power of repetitive transcranial magnetic stimulation (rTMS) and theta burst stimulation (TBS) in neurotransmitter modulation, receptor dynamics, and neuroimaging for neurological innovations. *Biomedicines.* **12**, 2506 (2024).
45. King, E. S. & Tang, A. D. Intrinsic plasticity mechanisms of repetitive transcranial magnetic stimulation. *Neuroscientist* **30**, 260–274 (2024).
46. Kays, J. L., Hurley, R. A. & Taber, K. H. The dynamic brain: Neuroplasticity and mental health. *J. Neuropsychiatry Clin. Neurosci.* **24**, 118–124 (2012).
47. Rehme, A. K. et al. Activation likelihood estimation meta-analysis of motor-related neural activity after stroke. *Neuroimage* **59**, 2771–2782 (2012).
48. Grefkes, C. & Fink, G. R. Connectivity-based approaches in stroke and recovery of function. *Lancet Neurol.* **13**, 206–216 (2014).
49. Cuypers, K. & Marsman, A. Transcranial magnetic stimulation and magnetic resonance spectroscopy: Opportunities for a bimodal approach in human neuroscience. *Neuroimage* **224**, 117394 (2021).
50. Zhang, Y. et al. Reproducibility of whole-brain temperature mapping and metabolite quantification using proton magnetic resonance spectroscopy. *NMR Biomed.* **33**, e4313 (2020).
51. Vilá-Ortiz, G. J. et al. The rate of tau synthesis is differentially regulated during postnatal development in mouse cerebellum. *Cell Mol. Neurobiol.* **21**, 535–543 (2001).
52. Kenny, T. C. et al. Cellular and organismal function of choline metabolism. *Nat. Metab.* **7**, 35–52 (2025).
53. Becktel, D. A. et al. Discovering novel plasma biomarkers for ischemic stroke: Lipidomic and metabolomic analyses in an aged mouse model. *J. Lipid Res.* **65**, 100614 (2024).
54. Xiong, X. Y. et al. Astrocyte-derived lactate aggravates brain injury of ischemic stroke in mice by promoting the formation of protein lactylation. *Theranostics* **14**, 4297–4317 (2024).
55. Zeng, X. et al. Bone marrow mesenchymal stem cells in a three-dimensional gelatin sponge scaffold attenuate inflammation, promote angiogenesis, and reduce cavity formation in experimental spinal cord injury. *Cell Transplant.* **20**, 1881–1899 (2011).
56. Xue, L. et al. Transplantation of human placental chorionic plate-derived mesenchymal stem cells for repair of neurological damage in neonatal hypoxic-ischemic encephalopathy. *Neural Regen. Res.* **19**, 2027–2035 (2024).
57. Dorsett, C. R. et al. Glutamate neurotransmission in rodent models of traumatic brain injury. *J. Neurotrauma* **34**, 263–272 (2017).
58. Imitola, J. et al. Directed migration of neural stem cells to sites of cns injury by the stromal cell-derived factor 1alpha/cxc chemokine receptor 4 pathway. *Proc. Natl. Acad. Sci. Usa.* **101**, 18117–18122 (2004).
59. Trigo, C. M. et al. Mesenchymal stem cell secretome for regenerative medicine: Where do we stand? *J. Adv. Res.* **70**, 103–124 (2025).
60. Haragopal, H. et al. Stemness enhancement of human neural stem cells following bone marrow msc coculture. *Cell Transplant.* **24**, 645–659 (2015).
61. Liu, G. et al. The effect of magnetic stimulation on differentiation of human induced pluripotent stem cells into neuron. *J. Cell Biochem.* **121**, 4130–4141 (2020).
62. Alvarez-Buylla, A. & Garcia-Verdugo, J. M. Neurogenesis in adult subventricular zone. *J. Neurosci.* **22**, 629–634 (2002).
63. Williamson, M. R. et al. Subventricular zone cytogenesis provides trophic support for neural repair in a mouse model of stroke. *Nat. Commun.* **14**, 6341 (2023).
64. Nakagomi, T. Unlocking the potential of regionally activated injury/ischemia-induced stem cells for neural regeneration. *Stem Cells* **43**, sxaf015 (2025).
65. Jurkowski, M. P. et al. Beyond the hippocampus and the svz: Adult neurogenesis throughout the brain. *Front Cell Neurosci.* **14**, 576444 (2020).
66. Fujiwara, S. et al. Administration of human-derived mesenchymal stem cells activates locally stimulated endogenous neural progenitors and reduces neurological dysfunction in mice after ischemic stroke. *Cells* **13**, 939 (2024).
67. Wang, T. et al. Recent advances in the mechanisms of postoperative neurocognitive dysfunction: A narrative review. *Biomedicines.* **13**, 115 (2025).
68. Rump, K. & Adamzik, M. Epigenetic mechanisms of postoperative cognitive impairment induced by anesthesia and neuroinflammation. *Cells* **11**, 2954 (2022).
69. Li, W. et al. Prospective association of general anesthesia with risk of cognitive decline in a Chinese elderly community population. *Sci. Rep.* **13**, 13458 (2023).
70. Tian, Y. et al. An ultraflexible electrode array for large-scale chronic recording in the nonhuman primate brain. *Adv. Sci. (Weinh.).* **10**, e2302333 (2023).
71. Badi, M. et al. Intrafascicular peripheral nerve stimulation produces fine functional hand movements in primates. *Sci. Transl. Med.* **13**, eabg6463 (2021).
72. Marshall, J. W. et al. Nxy-059, a free radical-trapping agent, substantially lessens the functional disability resulting from cerebral ischemia in a primate species. *Stroke* **32**, 190–198 (2001).
73. McEntire, C. R. et al. Impaired arm function and finger dexterity in a nonhuman primate model of stroke: Motor and cognitive assessments. *Stroke* **47**, 1109–1116 (2016).